茨城大学重点研究

「知的で持続可能な社会基盤および防災セキュリティ技術研究創出事業」

茨城大学工学部附属
防災セキュリティ技術教育研究センター

２０１４年度

報告書

茨城大学重点研究「知的で持続可能な社会基盤および防災セキュリティ技術創出事業」
平成 26 年度報告書刊行にあたって

プロジェクト代表　 呉　智深

本研究課題は，平成 23 年 4 月に課題募集プロポーザルとその審査により茨城大学重点研究課題として認定され，工学部，教育学部および茨城大学センター教員から構成される異分野研究者の集う場として活動が始まりました．本年度は活動 4 年目を迎えることとなりました．

この報告書では，学術誌論文をはじめとする研究成果に加えて，参加メンバーの学術企画の開催や参加，受賞例についても整理しましたが，「防災セキュリティ技術」という学際領域に類するテーマが示すように，昨年度に引き続き，多種多様な研究活動とその成果を収めてきたことが分かりました．

この重点研究課題で芽生えた研究成果は，平成 24 年 1 月に開所式が行われた工学部付属教育研究センター「防災セキュリティ教育研究センター」に引き継がれ，平成 25 年 4 月には，日本・中国・韓国各国の関係分野の先進的研究者が集う国際シンポジウムを土木学会茨城会と共催，平成 25 年 12 月には日本リモートセンシング学会国土防災リモートセンシング研究会主催 WS「次の大災害時に備えて、衛星画像の可能性」を後援(工学部)し，センターメンバーが主催側に参画しました.「教育と研究」双方の分野を対象として着実に成果を重ねつつあり，今後大型連携プロジェクトの獲得を含め、ますますの発展に向けて鋭意努力してゆく所存であります．

末筆とはなりますが，茨城大学重点研究課題として採択頂き，茨城大学を代表する研究課題の一つとして諸方面の応援と援助を頂きました茨城大学に心から感謝申し上げますとともに，必ずしも十分でなかった研究交流にも関わらず，本誌に示す多大なる研究成果を上げている参加メンバーに心から敬意と謝意を表します．

今後の研究活動への努力をお約束し，関連する皆様に感謝を申し上げますとともに，ここに平成 26 年度の研究成果を報告させて頂きます．

平成 27 年 3 月吉日
プロジェクト代表　 呉　智深

－目次－

Ⅰ．研究報告

Ⅱ.プロジェクト業績

Ⅰ.研究報告

（H26 年度参加教員発表の代表的な学術論文集）

Experimental Study on the Structural Performance of Concrete Bridge Columns Reinforced by Hybrid Steel and FRP Reinforcements

Arafa M. A. Ibrahim[1], Zhishen Wu [2*], Mohamed F. M. Fahmy[3], and Doaa Kamal[4]

Abstract: This paper presents the seismic performance of concrete bridge columns reinforced with hybrid steel and fiber reinforced polymer (FRP) reinforcements. A mechanical model describing the required damage-control performance of the proposed FRP-steel reinforced concrete (FSRC) structure is first discussed. A bond-based parametric experimental study was conducted on five FSRC bridge columns (using basalt FRP (BFRP) bars) and two reference steel-reinforced concrete bridge (SRC) columns to investigate the fundamental characteristics of the proposed reinforcement. All columns were tested under the combined effect of constant axial load and reversed cyclic loading. The investigated bond parameters included the texture of the FRP bars (smooth and ribbed); diameter of the FRP bars; location of the FRP bars with respect to the steel bars; and application of external FRP confinement. Different ductility and post-earthquake recoverability indices were applied to explore the effect of each design parameter on the performance of the proposed FSRC system. The experimental results show that RC bridge columns with both steel and FRP bars as longitudinal reinforcements could realize the existence of a stable hardening behavior (i.e., post-yield stiffness) as well as a reasonable displacement ductility of up to 10 before encountering strength degradation. Moreover, the number of FRP bars added for column longitudinal reinforcement did not have a substantial impact on the column elastic stiffness. The bond condition of the FRP bars to the surrounding concrete could be adopted as a design parameter because it had pronounced effects on the column failure mode, post-yield stiffness, residual displacement, and ductility. In addition, wrapping the plastic hinge region with an FRP jacket had a substantial effect on column ductility and energy dissipation.

CE Database subject headings: FRP bar; Basalt; Bridge; Column; Ductility; Recoverability; Damage control; Bond; Post-yield stiffness.

[1] Ph.D. Candidate, Dept. of Urban and Civil Engineering, Ibaraki University, 4-12-1 Nakanarusawa-cho, Hitachi 316-8511, Japan, E-mail: arafa_dem@yahoo.co.uk

[2*] Corresponding author, Professor, Dept. of Urban and Civil Engineering, Ibaraki University, 4-12-1 Nakanarusawa-cho, Hitachi 316-8511, Japan, E-mail: zswu@mx.ibaraki.ac.jp

[3] Assistant Professor, Dept. of Civil Engineering, Assiut University, Assiut, 71516, Egypt, E-mail: mfmf1976@yahoo.com

[4] MSc Candidate, Dept. of Urban and Civil Engineering, Ibaraki University, 4-12-1 Nakanarusawa-cho, Hitachi 316-8511, Japan, E-mail: 14nm826a@vc.ibaraki.ac.jp

Introduction

In recent seismic design philosophies of important bridges located in active seismic regions, quick post-earthquake recoverability of structural function has been considered in addition to ductility demand and energy dissipation (Kawashima 2000; Kawashima et al. 1998). Studies conducted by Kawashima et al. 1998; Christopoulos et al. 2003; Pettinga et al. 2007 showed that the post-yield stiffness ratio (i.e., the ratio of the post-yield stiffness to the initial elastic stiffness) of a bridge column is the main parameter controlling column residual displacement; for instance, at a given lateral displacement, a higher post-yield stiffness results in a smaller residual displacement. Priestley et al. 1996; Christopoulos et al. 2003; Wu et al. 2009 emphasized that the uncontrollable damage of conventional steel-reinforced concrete (RC) structures is due to the elasto-plastic characteristics of ordinary steel bars. Other studies (e.g., Dhakal and Maekawa 2002) reported that the main reasons for the non-ductile behavior of RC structures are the spalling of the cover concrete and buckling of the longitudinal reinforcement as a result of insufficient transverse reinforcement in the plastic hinge regions.

The damage level and residual displacement of bridge columns after an earthquake could be reduced by incorporating an unbonded-prestressed strand at the center of the column cross section (Ikeda et al. 2002; Zatar and Mutsuyoshi 2002; Sakai et al. 2006). Wu et al. 2009 proposed a steel- fiber reinforced polymer (FRP) composite bar (SFCB) as another technique that can be applied in the field of civil engineering to combine the advantageous mechanical and physical properties of both steel and FRP composites, the high elastic modulus and good ductility of a common steel bar and the good anti-corrosion ability and elasticity of FRP composites. This bar consisted of an inner steel core and outer longitudinal continuous fiber layer. Reinforcing RC bridge columns with steel-fiber composite bars enabled the mitigation of their residual displacement and the control of their post-yield stiffness (Fahmy et al. 2010). Moreover, analytical and experimental studies on this reinforcing material showed that the post-yield stiffness depends on the properties of the fibers used, whereby columns reinforced with steel-basalt fiber composite bars exhibited a larger drift capacity before the rupture of the basalt fibers than those reinforced with steel-carbon fiber composite bars (Fahmy et al. 2010). Although scale model columns reinforced with this type of composite bars exhibit a favorable seismic performance with damage-controllable states after yielding, the production of comparable composite bars for practical application with larger inner steel cores may require an excessive amount of outer longitudinal fiber material, which would complicate the production process; thus, using many composite bars with a smaller inner steel core would be necessary. In addition, the bond performance between composite bars and concrete must be further improved .

The objective of this study is to investigate the application of both steel and FRP bars as a longitudinal reinforcement in earthquake-resisting structural elements. To achieve this objective, a design guideline in light of both current code provisions and a proposed damage control performance was followed to define the design details of steel-FRP reinforced columns. The bond between the FRP bar and surrounding concrete, as a key parameter that could affect column performance, was examined by using FRP bars with different textures and diameters. In addition, the effect of replacing some of the transverse steel reinforcement with external FRP confinement was examined. The efficiency of the proposed reinforcement design and the role of different parameters were investigated in a detailed experimental program considering the effect of both constant axial load and horizontal cyclic loading tests on RC bridge square columns.

FRP-Steel RC Structure

Because post-yield stiffness is the main factor that influences the strength demand, seismic stability, and residual displacement of RC structures (Iemura et al 2006; Christopoulos and Pampanin 2004), it is important to develop a tool to control the structural post-yield stiffness. General guidelines and design equations for longitudinal and transverse steel reinforcement of concrete bridges to achieve high ductility and dissipate sufficient energy before failure have been well defined in current design codes. The specifications of the current design codes can produce RC structures that can withstand severe earthquakes; however, the elasto-plastic characteristics of steel reinforcement would cause difficulty in quickly recovering structural functions after an earthquake. In this study, FRP composites are proposed to be added to the longitudinal reinforcement in RC bridge columns because merging the elastic characteristics of FRP composites with conventional steel reinforcement could provide the structure with the desired post-yield stiffness.

In this regard, two conventional steel-reinforced concrete (SRC) bridge structures, SRC1 and SRC2, were first tested. SRC1 was designed to withstand moderate earthquakes, whereas SRC2 was designed to resist a massive earthquake. Compared with SRC1, an additional increase in the concrete dimensions and/or steel reinforcement is necessary in SRC2. However, with the elastic characteristics of FRP composites, it would be possible to increase the lateral resistance of SRC1 to the required level without an increase in the column steel reinforcement or concrete dimensions by adding longitudinal and transverse FRP composites to the original SCR1. Fig. 1 compares the schematic reinforcement model for the proposed FSRC structure and that of the conventional SRC structures. The proposed FSRC structure is the conventional steel RC structure with the addition of longitudinal FRP reinforcement (FRP bars) and transverse FRP reinforcement (FRP sheets applied as a continuous jacket or separated strips).

A detailed mechanical model of the proposed FSRC structure, Fig. 2, is addressed here in comparison with the two SRC structures. This model is a modified form of the proposed damage control model for existing RC structures retrofitted with FRP composites (Fahmy et al. 2009), where further developments meeting the requirements of modern codes for new structures are considered. As shown in Fig. 2, the idealized lateral load-deformation response of the proposed system (FSRC) goes along the path represented by O-C-Y-M-S-F, whereas the performances of the two conventionally reinforced concrete bridges (SRC1 and SRC2) are represented by O-C_1-Y_1-M_1-F_1 and O-C_2-Y_2-M_2-F_2, respectively. The proposed system using FRP-steel reinforcement is designed for the life safety performance objective to withstand moderate earthquakes with its elastic performance and exhibit the demand strength of a strong earthquake to ensure the existence of a stable post-yield stiffness. Prior to the yielding of the steel reinforcement, structures SRC1 and FSRC share similar initial elastic stiffnesses, K_1, whereas SRC2 exhibits a higher elastic stiffness. The higher yield stiffness of the structure would lead to a shorter vibration period and increase the earthquake forces received (Saiidi et al. 2009). Beyond the yielding of the SRC structures, the deformations of both SRC1 and SRC2 increase dramatically, whereas the increase in the lateral load is insignificant. In other words, SRC demonstrates a small post-yield stiffness along lines Y_1-M_1 and Y_2-M_2 (see Fig. 2). In contrast, the proposed FRP-steel system ensures the gradual increase in lateral resistance up to the demand strength of a strong earthquake along line Y-M such that the system could realize the existence of a considerable post-yield stiffness, K_2. Beyond the yielding point, SRC systems experience extensive straining of the steel reinforcement to achieve the required ductility; thus, after peak loading (and a stability zone in some cases), the earthquake-resisting structural elements are subject to significant damage, e.g., major spalling of the concrete cover and buckling of the main steel reinforcement. The failure point of the SRC system corresponds to a 20% reduction in the maximum achieved lateral strength, points F_1 and F_2 for SRC1 and SRC2, respectively. Compared with the SRC system, the proposed system is characterized by a clear stability zone of the peak strength (zero stiffness (K_3)) along line M-S, whereby the structure demonstrates the desirable ductile performance before the strength degradation. Furthermore, the FRP elements used are employed as a fuse-resisting element to be replaced after a strong earthquake to restore the original structural function. Therefore, the failure point of this system is defined when the contribution of the FRP elements to the lateral resistance is completely lost along path S-F (negative stiffness (K_4)).

The performance of the proposed FRP-steel system can be divided into four distinctive zones according to the earthquake level and damage level. Zone 1, from points O to Y: through this zone, the structure may be attacked by small-to-moderate earthquakes without experiencing any pronounced damage, and after an earthquake, the original function of the structure can be restored without any repair or replacement of elements. Zone 2, from points Y to M: through this zone, under a strong earthquake, the damage can be effectively controlled by the secondary stiffness (Fahmy et al. 2009). The original function of the structure can be quickly recovered through minor repair work on damaged structural elements while the structure is open to all traffic. Zone 3, from points M to S, is where a desired ductility after hardening under a large earthquake should be achieved. In this zone, damage to the substructural elements, such as major spalling of the concrete cover, may occur, but the proposed system can be maintained without collapse. The original function of the structure may also be recovered by repairing damaged parts of the concrete and replacing FRP reinforcement elements. In this zone, the structure can be used by emergency vehicles for life-saving purposes. Ultimately, through Zone 4 from points S to F, only the FRP reinforcement (earthquake-resistant elements) of the substructural elements (columns) would be damaged until its contribution to the lateral strength fully vanishes. In this stage, limited access to service shall be permitted until structural function is completely recovered via the replacement of damaged elements.

To this end, the proposed structural system using steel and FRP reinforcement has several advantages with respect to the counterpart steel-reinforced structural system. The initial stiffness is smaller than that of steel-reinforced bridges (SRC2), and therefore, a considerable reduction in the seismic force input into the structure can be achieved. Second, the existence of the stable post-yield stiffness controls the lateral deformation after yielding and reduces the residual displacement (permanent deformation) after an earthquake.

Experimental Program

An experimental investigation on concrete bridge columns reinforced with both FRP and steel reinforcement was conducted. One column (CS-2%) was designed as a reference for a RC bridge column that can safely resist moderate earthquakes, while another column (CS-4%) was considered to resist nearly twice the lateral force of the first column. A complete design was also provided for a concrete column with the same concrete parameters and steel reinforcement of CS-2% in addition to FRP reinforcement. The following section describes the design parameters of both the steel and FRP reinforcements.

Design of the Proposed Steel and FRP Columns

Design of Steel RC Columns

A cantilever bridge column with an overall height of 1.0 m, a cross section of 200x200 mm, and a distance from the column base to the point of the lateral load application of 850 mm, yielding an aspect ratio of 4.25, was proposed for this experimental study. A target compressive strength

(f_c') of 30 MPa was applied to all examined columns. The yield strength (f_y) and ultimate strength of the 13-mm-diameter deformed steel bars used as longitudinal reinforcements were 375 and 560 MPa, respectively, and the corresponding values for the 6-mm-diameter steel transverse reinforcements were 400 and 625 MPa, respectively (see Table 1). Before applying the proposed cyclic loading that will be explained later, an axial load of approximately 40 kN, inducing an axial compression stress of 1 MPa (Zatar and Mutsuyoshi 2002), was applied on all column specimens. Using the aforementioned data, details of the conventional reinforced steel columns were defined as follows:

Longitudinal Steel Reinforcement

AASHTO 2012 specifies that the area of the longitudinal reinforcement (A_l) of columns located in a high-seismic-hazard area is to be no less than 0.01 or more than 0.04 times the gross cross-sectional area A_g (i.e., $0.01 \leqslant \rho_l \leqslant 0.04$, where ρ_l is the steel reinforcement ratio and equal to A_l / A_g). In this study, the first steel-reinforced column (CS-2%) used six longitudinal steel bars of 13-mm-diameter (i.e., ρ_l=2%), whereas the second column (CS-4%) was reinforced with twelve steel bars of 13-mm-diameter (i.e., $\rho_l=\rho_{l\ \max}$=4%, where $\rho_{l\ \max}$ is the maximum steel reinforcement ratio). The theoretical strengths of these two samples were 36.0 and 67 kN, respectively, and both values were defined using the AASHTO 2012 rectangular stress block for concrete in compression, which has a mean stress of $0.85f'_c$ and an ultimate concrete compression strain of 0.003, and a steel stress of f_y for the longitudinal steel bars.

Transverse Reinforcement

To ensure a ductile reinforced concrete column, it is critical to provide the plastic hinging regions with transverse reinforcement to confine the concrete core, prevent early buckling of the longitudinal reinforcement, and ensure a dominant flexural failure mode. To achieve the specified demand displacement ductility, Wehbe et al. 1999 proposed Eq. 1 to define the required transverse reinforcement as follows:

$$A_{sh} = 0.1\mu_{\Delta}\sqrt{\frac{f_{cn}}{f_c'}}S_h h_c\left[0.12\frac{f_c'}{f_{yh}}\left(0.5 + 1.25\frac{P}{f_c' A_g}\right) + 0.13\left(\rho_l\frac{f_{yl}}{f_{sn}} - 0.01\right)\right] \qquad (1)$$

where A_{sh} is the area of transverse reinforcement in each of the transverse directions, h_c is the dimension of the concrete core of the section measured perpendicular to the direction of the hoop bars to the outside of the perimeter hoop, S_h is the center-to-center vertical spacing of the hoops not exceeding 4.0 in, A_g is the gross area of the column cross section, f_{cn}=27.6 MPa, f_{sn}=414 MPa, f_{yl} is the yield stress of longitudinal steel reinforcement, f_c' is the concrete compressive strength, P is the axial load, and μ_{Δ} is the demand displacement ductility factor.

Using Eq. (1) and assuming a displacement ductility demand before failure of μ_{Δ} <10 (Wehbe et al. 1999), the transverse reinforcement required was 6-mm-diameter stirrups with a spacing of 50 mm. With reference to the design provisions of AASHTO 2012, it would be reasonable to use 6-mm-diameter stirrups with a spacing of 25-mm- or 8-mm-diameter stirrups with a spacing of 50 mm. The transverse reinforcement defined by AASHTO 2012 is independent of the column reinforcement ratio. From a practical perspective, because the amount of transverse reinforcement defined by Eq. (1) could achieve this level of ductility, replacement of some of the inner transverse steel reinforcement (based on AASHTO 2012) with external FRP jacket would increase the concrete cover’s compressive strength. Therefore, for all columns, the transverse steel reinforcement was determined based on Eq. 1, which is nearly 60% of the stirrups required by AASHTO 2012. Moreover, an external BFRP jacket was provided in some experimental cases to develop the same shear strength with the reduced amount of transverse steel reinforcement. By using an FRP sheet with the mechanical properties shown in Table 1, it was found that wrapping the plastic hinge region of the columns with a 0.666-mm-thick FRP jacket would compensate for the decrease in shear strength and provide a good confinement to the concrete cover.

Design of FRP-Steel RC Columns

The FRP-steel RC (CSF) column had the same steel reinforcement as column CS-2% (6 steel longitudinal bars of 13-mm diameter and steel stirrups of 6-mm diameter spaced at 50 mm), which would result in a flexural strength of 36.0 kN, as stated previously. Therefore, additional FRP bars were added to reach a strength comparable to that of column CS-4% (67.0 kN). Among all available types of FRP materials, basalt fiber (BFRP) shows advantageous mechanical and chemical characteristics and a high performance-to-cost ratio. For instance, BFRP has a higher strength and modulus, a similar cost, and a greater chemical stability than E-glass FRP; a wider range of working temperatures and lower cost than carbon FRP (CFRP); and a five-fold higher strength and approximately one-third the density of commonly used low-carbon steel bars (Wu et al. 2010; Sim et al. 2005; Palmieri et al. 2009). Due to the above advantages, BFRP bars were used to investigate the proposed FRP-steel RC design. Using BFRP bars with a tensile strength and elastic modulus of 1,120 MPa and 48 GPa, respectively, as shown in Table 1, four BFRP bars of 10-mm diameter or six BFRP bars of 8-mm diameter would increase the column strength to the desired value. To prevent problems of plastic hinge relocation, anchorage failure, or other failure modes, the BFRP bars in this study were extended to a height of 700 mm from the column base and embedded in the column footing to a depth of 300 mm.

Test Specimens and Experimental Parameters

Seven different column units were prepared to investigate the efficiency of the proposed reinforcements. All column units had a deep concrete base of 1.0 x 0.5 x 0.5 m (length x width x depth), which simulated a rigid foundation for the tested column. Due to its roles in acting as a foundation and resisting the action induced by applied loads, the concrete base was provided with heavy reinforcement to ensure its elastic performance during the tests of all columns. Similar to the steel RC column, its cross-section was 200 x 200 mm, and its height was 1,000 mm. The distance from the column base to the point of the application of the lateral load was 850 mm, with an aspect ratio of 4.25. To avoid any unexpected local failure at the loading region, the transverse steel reinforcements were spaced at 30 mm in the highest 300 mm portion of the column units. All columns were attached to a strong steel floor using four vertical high-strength steel rods. The geometry and instrumentation of a typical column unit are shown in Fig. 3.

The test specimens were designed such that the effect of a series of parameters on the seismic response of the proposed concrete bridge columns could be investigated. These parameters include the type of reinforcement (ordinary steel bars only or both steel and FRP bars); diameter of the FRP bars (10 mm or 8 mm); texture of the FRP bars (smooth or rough texture); location of the FRP bars in the tension and compression cross-section sides (internally in the same fibers as the longitudinal steel bars, or externally in the concrete covers); and use of FRP jacketing (with or without). A detailed description of the test specimens follows and is supported by Figs. 3, 4 and 5 and Table 2:

- Specimen CS-2% (Fig. 4.a) served as a reference specimen for the steel RC columns. In this column, the longitudinal steel reinforcement consisted of six 13-mm-diameter bars (i.e., ρ_l=0.02), and the transverse reinforcement consisted of 6-mm-diameter internal closed stirrups spaced every 50 mm;
- Specimen CS-2%-J (Fig. 4.b) was reinforced with the same steel reinforcement as specimen CS-2%. In addition, BFRP jacketing was provided to the plastic hinge region of this column,

where a jacket of 0.333-mm thickness was applied to the lowest 300 mm of the column (i.e., L_{j1}=300 mm) and then another jacket of 0.333-mm thickness was added to only the lowest 200 mm of the column portion (i.e., L_{j2}=200 mm);

- In addition to the steel reinforcement details of column CS-2%, specimen CSF-2.8%-IS-D10 (Fig. 4.c) was reinforced with two 10-mm-diameter BFRP bars placed on each of two opposite sides of the column (those with the highest tension/compression) at the same place as the longitudinal steel bars. The surface texture of the BFRP bars contained small prefabricated indentations (factory product), as shown in Fig. 5.b. By adding the FRP bars to the steel bars, the resulted reinforcement ratio was nearly 2.8% (i.e., ρ_l=0.028);
- Specimen CSF-2.8%-IS-D10-J (Fig. 4.d) was similar to specimen CSF-2.8%-IS-D10 but wrapped at the plastic hinge region with the same BFRP jacketing as in column CS-2%-J;
- Specimen CSF-2.8%-IR-D10-J (Fig. 4.d) was the same as specimen CSF-2.8%-IS-D10-J, but the surface texture of the BFRP bars was spirally roughened with BFRP strips in two perpendicular directions, as shown in Fig. 5.c;
- Specimen CSF-2.8%-ES-D10-J (Fig. 4.e) was the same as specimen CSF-2.8%-IS-D10-J, but the BFRP bars were placed outside of the steel stirrups, i.e., in the concrete cover. In addition, BFRP jacketing was provided to the plastic hinge region of this column, where a jacket of 0.333-mm thickness was applied first to the lowest 600 mm of the column portion (i.e., L_{j1}=600 mm) and then another jacket of 0.333-mm thickness was added to only the lowest 200 mm of the column portion (i.e., L_{j2}=200 mm); and
- Specimen CSF-2.8%-ES-D8-J (Fig. 4.f) was reinforced with both steel and FRP reinforcement and wrapped with the BFRP jacketing as in specimen CSF-2.8%-ES-D10-J, but the FRP reinforcement consisted of three 8-mm-diameter BFRP bars placed external to

the steel stirrups on each of two opposite sides of the column (those with the highest tension/compression) in the concrete cover. The surface texture of the BFRP bars contained small indentations, as shown in Fig. 5.a. The total reinforcement ratio in this column was approximately 2.8% (i.e., ρ_l=0.028).

Loading and Instrumentation

All columns were subjected to a constant axial load of 40 kN and several excursions of lateral cyclic loading applied at 850 mm above the column base using a dynamic actuator with a capacity of 700 kN. The reversed cyclic loading sequence was determined based on the column displacement at the yielding load (Δy), which was numerically defined for the reference column and kept the same for all specimens. The lateral loading sequence started with two cycles of 0.5Δy followed by two cycles of Δy and then three cycles each of 2Δy, 3Δy, 4Δy, 6Δy, 8Δy, and 10Δy until failure. A linear variable differential transformer (LVDT) was used during testing to record the horizontal displacement of the tested columns. The axial strain histories for both the steel and FRP reinforcements were recorded during the test by using a set of 5-mm-long strain gauges, arranged as shown in Fig. 6. Although efforts were made to keep the axial load constant during the experimental tests, laterally displacing the columns resulted in some variations in the axial load, particularly at high levels of lateral displacement. The actual applied axial load was in the range of 40 to 100 kN during the tests. All installed instrumentation are shown in Fig. 3.

Experimental Results and Discussion

General Observations and Hysteretic Curves

In this section, the results of each column specimen are individually discussed with reference to its hysteretic response (V-δ curve) and failure mode. Fig. 7 shows the lateral load versus the column drift ratio for all tested columns, and Fig. 8 shows the final failure mode of these columns. The deformation capacity of the columns is expressed as the member lateral drift, which is defined as the ratio of the lateral displacement at the point of the load application of each column to the effective height of the column (850 mm). The longitudinal strains of the FRP bars are also examined, where the lateral load-FRP bar strain hysteresis loops were recorded by the FRP bar's strain gauge in each column, as shown in Fig. 9. Table 3 summarizes the characteristic values and experimental findings in both the positive and negative loading directions together with the observed failure mode of each specimen, and Table 4 contains the average characteristic values of both directions. The terms V_{cr} and V_y represent the cracking load and steel yielding load, respectively, and the terms δ_{cr} and δ_y represent the corresponding lateral displacements. The cracking load and corresponding displacement were approximately defined from the first turning points of the load-displacement curves when the plastic hinge zone was covered with an FRP jacket. The yielding loads and displacements were obtained from the results of the strain gauges attached to the longitudinal steel bars. The term V_P represents the peak load, and it is characterized by two displacement values δ_{P1} and δ_{P2}, where δ_{P1} corresponds to the peak load and δ_{P2} corresponds to the end of the plateau zone, if any. The terms V_u and δ_u represent the ultimate load and its corresponding displacement, respectively, and they were defined for SRC specimens at the drift level at which the load capacity decreased to 80% of the peak load. For the other columns (FSRC columns), the ultimate loads and displacements were defined at the degradation of the peak load to the peak load of the SRC column, column CS-2%. Values of the displacement ductility factor, μ, at different characteristic points were superimposed on the hysteretic responses, as shown in Figs. 7 and 9, where $\mu=\delta/\delta_y$ and δ=lateral displacement at the load application point. Moreover, a complete description of the failures noted during the loading of all columns was included in the hysteretic curves using marked footnotes. The following sections provide a detailed discussion of the behavior of all tested columns.

Columns Reinforced with Steel Bars (SRC Columns)

For the control specimen CS-2%, flexural cracks first occurred near the column base in the first loading cycle at a drift level of approximately 0.1%, corresponding to a lateral load of 9.2 kN. While displacing the specimen in both loading directions, new horizontal and slightly inclined cracks formed and propagated with further loading and distributed in the lowest 300 mm of the column in both loading directions. The first yielding of the steel bars was observed at a drift level of 0.65%, corresponding to a lateral load of 26.0 kN, as shown in Fig. 7.a. Afterward, a stable hardening cyclic response appeared and continued up to a drift level of 3.5% (μ =5.3), corresponding to an average peak load of 37.5 kN in both the push and pull directions. Following this drift level, a peak-loading horizontal plateau was formed with the appearance of significant wide cracks in the plastic hinge regions up to a drift level of 5.9% (μ=8.8). A bulking of the concrete covers accompanied with a smooth degradation of the cyclic response after this level took place up to a drift level of 7% (μ=10.3). Beyond this level, a complete spalling and crushing of the concrete cover within a height of approximately 200 mm above the column footing occurred. After the spalling of the concrete cover, a serious buckling of the longitudinal reinforcement, Fig. 8.a, was observed, causing a sudden drop in the lateral load and terminating the test.

For specimen CS-2%-J, the behavior was significantly affected by wrapping the plastic hinge region with the FRP jacket (see Figs. 7.b and 8.b). The use of the BFRP jacket prevented the crack propagation from being observed, but the load-displacement curve demonstrated that the first turning point, indicating the first cracking, was at a drift level and corresponding lateral load nearly the same as those of the control specimen. The first yielding of the steel reinforcement took place at a drift level of 0.64%, corresponding to a lateral load of 27.2 kN (i.e., V_y=1.05 V_{yc}, where V_{yc} is the yielding load of column CS-2%). After the yielding of the steel bars, the column was able to continue carrying a load in a stable manner up to a drift level of 5.9% (μ=8.9), corresponding to a peak lateral load of 43.4 kN (i.e., V_P=1.15V_{PC}, where V_{PC} is the average peak load of column CS-2%). Beyond this drift, a gradual bulging of the FRP jacket accompanied by a smooth gradual loss of strength took place up to an average lateral drift of 9.4% (μ=14.3), corresponding to a lateral load of 40.8 kN. Upon increasing the lateral displacement beyond this drift level, the bulging of the FRP jacket was accompanied by a local buckling of the steel bars within a height of approximately 100 mm above the column footing, followed by the rupture of some steel bars, as shown in Fig. 8.b.

Columns Reinforced with Hybrid Steel and FRP Reinforcements (FSRC Columns)

Prior the yielding of the steel bars, the observed behavior of all FSRC columns was slightly affected by the contribution of the FRP reinforcement. This could be due to the small contribution of the FRP bars to both the column strength and deformation, and this was identified from the average longitudinal strain records of BFRP bars located at both loading sides, which ranged from 8.5% to 11% of the uniaxial rupture strain of the BFRP bars (i.e., ε_{fy}=0.085 to 0.11 ε_r, where ε_{fy} is the average strain recorded in the FRP bars at the yielding of the steel bars and ε_r is the rupture strain of the BFRP bar). This small contribution is due to the small elastic stiffness ratio between FRP and steel (i.e., $A_f\, E_f/A_S\, E_S$=0.095, where A and E are the gross cross-sectional area and elastic modulus, respectively, and subscripts S and f denote the steel and FRP bars, respectively). Beyond the yielding of the steel bars, the contribution of the FRP reinforcement became significant and controllable, where a hardening zone with a clear positive post-yield stiffness was realized. Compared to the control specimen, all specimens reinforced with both steel and FRP bars achieved considerably higher lateral strength (i.e., 30-85% higher than that of column CS-2%). In contrast to the control column, the failure modes of all FRP-reinforced specimens were never attributed to the buckling of the internal reinforcement, as a significant portion of the total force in the compression zone was carried by the FRP bars. However, buckling of the longitudinal internal bars occurred abruptly after bond or rupture failure of the FRP bars. The main observations of the behavior of such columns are described in detail in the following paragraphs.

Columns Reinforced with 10-mm-diameter BFRP Bars

For column CSF-2.8%-IS-D10, small cracks were first observed during the first loading cycle near the column base. With further loadings, these cracks increased and distributed within the lowest 300 mm of the column height. The applied strain gauges recorded a first yielding strain of the steel bars at a drift level of 0.74%, corresponding to a lateral load of 27.6 kN. As shown in Fig. 7.c, beyond the yielding of the steel bars, the column continued carrying loads with a stable post-yield stiffness up to a lateral drift of 3.5% (μ=4.2), corresponding to a peak load of 48 kN (V_P=1.28V_{PC}) in one loading direction. In the other loading direction, a peak lateral load of 50.5 kN (V_P=1.35V_{PC}) was reached at a drift of 4.7% (μ=5.6). During this hardening zone, a considerable propagation of cracks appeared and further widened. After reaching the peak load, the concrete cover at the column footing interface and above it started to bulk out, causing a plateau at the peak load level. Along this plateau, concrete crushing and spalling became significant, particularly within the first 200 mm near the column footing. A “popping” sound was heard during the loading of the column to a lateral drift of 7% (μ=8.5), at which the measured strain ε_f of the BFRP bars was 0.47ε_r, indicating the first local bond failure between the FRP bars and surrounding concrete at the column-footing interface. At this drift level, a 20% decrease in the load capacity occurred, confirming the effect of slippage between the FRP bars and surrounding concrete. An additional degradation in the column strength of 5% up to the completion of the first loading cycle to a lateral drift of 8.2% (μ=9.9) was also observed. A "popping" sound was heard again when loading to the second and third cycles of the same lateral drift, together with separation of the concrete from the footing, which clearly indicated another local bond failure of the FRP bars. The strain of the FRP bars at this drift level was approximately 54% of the rupture uniaxial strain (i.e., ε_{fy}=0.54 ε_r), as shown in Fig. 9.c. However, as a result of the applied cyclic loading, the partial rupture of the BFRP bars was observed within the first 100 mm above the column base. Consequently, another 40% decrease in the carried load occurred. Hence, all of the stresses in the longitudinal direction were carried by the steel bars, resulting in a sudden local buckling of some of them and subsequently their rupture. Fig. 8.c shows the state of column CSF-2.8%-IS-D10 just before the rupture of the steel bars.

Figs. 7.d, 8.d, and 9.d show that the observed trim of the behavior of specimen CSF-2.8%-IS-D10-J was similar to that of specimen CSF-2.8%-IS-D10 up to a high loading level. The first yielding of the steel bars was recorded at a lateral load of 28.1 kN, corresponding to a drift of 0.6%. The column achieved a peak load of 56.75 kN (V_P=1.51V_{PC}) at a drift level of 5.9% (μ=6.8) in one loading direction and a peak load of 59 kN (V_P=1.57V_{PC}) at a drift of 4.7% (μ=5.4) in the opposite loading direction. Beyond the peak load, a stability in this load was observed up to a drift level of 7% (μ=8.1), at which point the first bond failure of the FRP bars occurred, causing an average decrease of 15% in the lateral load. Beyond this deformation level, the column maintained the remaining lateral load up to a drift level of 8.2% (μ=9.5), at which point a complete debonding of the FRP bars occurred, accompanied by another drop in the lateral load by approximately 20%. As a consequence, the steel bars became vulnerable to high stresses, resulting in local buckling and subsequent rupture of some of them, causing a termination of the column test, as shown in Fig. 8.d. The maximum achieved strain in the FRP bars before the bonding failure was approximately 56% of the rupture strain, as shown in Fig. 9.d.

The response of column CSF-2.8%-ES-D10-J shows the effect of placing FRP bars out of the transverse reinforcement in the concrete cover (see Fig. 7.f). Compared to CSF-2.8%-IS-D10-J that was internally reinforced with FRP bars, a slight increase in the carried lateral load could be achieved. This increase was attributed to the increase in the effective depth of the FRP bars (i.e., the distance from the fibers of the maximum compression strain to the center of the FRP bars located on the tensile side). As shown in Fig. 7.f and summarized in Table 3, the first yielding of steel bars was recorded at a drift level of 0.67%, corresponding to a lateral load of 33.2 kN. Beyond the yielding of the steel bars, the column showed a gradual increase in the carried lateral load in both loading directions up to drift levels of +4.7% (μ=6.7) and -5.9% (μ=8.6), corresponding to lateral loads of +63 kN (V_P=1.68V_{PC}) and -60 kN (V_P=1.6V_{PC}), respectively. Afterward, local bond failure of the FRP bars occurred as the bond stress between the FRP bars and surrounding concrete reached the bond strength. Two successive drops of the lateral load were observed in both loading directions, where the lateral load in the two loading directions at a drift level of 9.4% (μ=10.3) reached values of +37.5 and -38.3 kN. Before the debonding of the FRP bars, the recorded strain was approximately 61% of the rupture strain, as shown in Fig. 9.f. The presence of the FRP bars outside the closed stirrups resulted in a pronounced rupture of the external fibers of the BFRP bars, particularly after the bulging of the BFRP jacket, as shown in Fig. 8.f.

Specimen CSF-2.8%-IR-D10 examined the effect of roughening the texture of the BFRP bars on the bond between the FRP bars and concrete. Fig. 7.e and Table 3 show that the first yielding of steel bars was at a lateral drift of 0.69%, corresponding to a lateral load of 28.1 kN. Beyond the yielding of the steel bars, a hardening zone of this column was realized in a manner quite similar to that in column CSF-2.8%-IS-D10, with smooth FRP bars, up to a drift level of 3.5%. After this lateral drift ratio, the hysteretic loops showed a continuous increase in column strength but with a smaller positive stiffness in both loading directions up to the completion of the first loading cycle of the lateral drift of 8.2% (μ=11.3), corresponding to lateral loads in the positive and negative directions of 60 kN (V_P=1.6V_{PC}) and 69 kN (V_P=1.84V_{PC}), respectively. Displacing the column in the two directions with the additional two loading cycles to the same lateral drift resulted in an approximately 25% loss in the achieved peak lateral strength. This drop was mainly due to a complete rupture of the FRP bars at 50 mm above the column base, as shown in Fig. 8.e. At this loading stage, a loud sound was heard, and a bulge formed in the BFRP jacket. During the loading process, the strain gauges located at the section of maximum moment failed early, and only the strain gauge located at 150 mm height continued until the rupture of the BFRP bars. The maximum attained axial strain of the FRP bars recorded by this strain gauge was approximately 71% of the uniaxial rupture strain, as shown in Fig. 9.e. Following the rupture of the FRP bars, a sudden increase in the stresses were experienced by the steel bars, causing some of them to rupture.

Columns Reinforced with 8-mm-diameter BFRP Bars

The observed behavior of specimen CSF-2.8%-ES-D8-J was highly similar to that of the column reinforced with rough BFRP bars; this could be attributed to good bond conditions between the FRP bars and surrounding concrete in both cases. As shown in Fig. 7.g and Table 3, the first yielding of the steel bars was recorded at a drift level of 0.65%, corresponding to a lateral load of 31.9 kN. Beyond the yielding of the steel bars, this column achieved the largest lateral resistance among all tested columns, where at a drift of 7% (μ=10.3), the maximum attained lateral strengths in the positive and negative directions were 68 kN (V_P=1.81V_{PC}) and 71 kN (V_P=1.89V_{PC}), respectively. At this drift level, a loud sound was heard, indicating the probability of rupture of one or more FRP bars, followed by an approximately 15% decrease in the peak load. The column was then able to maintain its achieved strength up to a lateral drift of 8.2%, at which point a second loud sound was heard, indicating the probability of rupture of the additional FRP bars, accompanied with another 25% decrease in the lateral load, after the completion of the second loading cycle at this drift level. Unfortunately, the results of the third loading cycle at this drift level were lost during the transfer of the data from the logger. The continued displacement of the column led to a rupture of some steel bars. The results of this column indicated that the FRP bars fulfilled nearly 94% of its rupture strain before failure, as shown in Fig. 9.g. Moreover, after removing the FRP jacket at the lowest part of the column, the decreases in the lateral load were confirmed to be due to the rupture of the FRP bars, as shown in Fig. 8.g.

Envelope Responses

The average skeleton curves of push and pull loading directions of all tested specimens are presented in this section. To investigate the effect of each tested parameter individually, the skeleton curves of all specimens are shown in five separate figures, where the effect of each parameter can be investigated in one figure, as shown in Fig. 10. Referring to sec. 2, the effectiveness of the proposed column reinforcement should be evaluated in light of the targeted mechanical load-displacement model. To this end, the evaluation process is presented in this section in terms of initial stiffness, post-yield stiffness, and ductility measurements, as shown in

Table 5. To draw firm conclusions, the response of the steel RC column (CS-4%), discussed earlier, was numerically simulated using the OpenSees software (Mazzoni et al.). The experimentally applied cyclic loading regime was adopted in the numerical simulation to predict the behavior of column CS-2% for comparison with the experimental results (see Fig. 10.a) and then to predict the performance of column CS-4%. Only the envelope response of the hysteretic curve is presented here for comparison with the FSRC columns.

Initial Stiffness

The initial stiffness or elastic stiffness (K_1) is an important seismic performance measure (index) that can be evaluated as $K_1=V_y/\delta_y$. In comparison cases, higher values of this index would lead to a shorter vibration period of the structure and would generally increase the earthquake forces received (Saiidi et al. 2009). K_1 was determined for all tested specimens to investigate the effect of adding FRP reinforcement to the steel reinforcement, as shown in Table 5.

As shown in Fig. 10 and summarized in Table 5, adding FRP composites to the steel reinforcement resulted in an insignificant change in the initial stiffness values. Although wrapping the plastic hinge region with an FRP jacket resulted in a significant enhancement in the column confinement, the increase in the initial stiffness was extremely small; K_1 of column CS-2%-J=1.06 K_1 of column CS-2%, and K_1 of column CSF-2.8%-IS-D10-J=1.07 K_1 of column CSF-2.8%-IS-D10. Placing additional FRP bars for further transverse reinforcement had no clear effect on the initial stiffness compared with the reference column CS-2%, whereas adding FRP bars of 8- or 10-mm diameter in the concrete cover (outside the transverse reinforcement) resulted in an approximately 20% increase in the initial stiffness. Moreover, the bond condition between the FRP bars and concrete showed no considerable effect on the initial stiffness; K_1 of column CSF-2.8%-IR-D10-J ≅ K_1 of column CSF-2.8%-IS-D10-J, and K_1 of column CSF-2.8%-

ES-D8-J ≅ K_1 of column CSF-2.8%-ES-D10-J. In contrast, Fig. 10.b and Table 5 show that the initial elastic stiffness of the numerically investigated column CS-4% was over twice that of the control specimen. That is, increasing the column strength to withstand a strong earthquake using additional steel reinforcement would greatly affect the elastic stiffness and in turn its vibration period, whereas adding FRP bars to an RC structure would be a reasonable solution to avoid any increase in the imposed seismic force on the structure.

Post-Yield Stiffness

In previous studies on damage-controlled structures, e.g., Kawashima et al. 1998; Christopoulos et al. 2003; Pettinga et al. 2007, the residual deformations are dependent on the post-yield stiffness ratio. For instance, when two structures attained a comparable lateral displacement, a smaller residual displacement would be obtained for the structure with the higher post-yield stiffness ratio. Therefore, the post-yielding stage of the tested columns up to the column peak strength was evaluated using two post-yield stiffness indices. The first index was the ratio between the column post-yield stiffness and elastic stiffness (k=k_1/k_2 %), where the starting point of the post-yield stiffness of all tested columns was defined as the theoretical strength of the control specimen CS-2% defined previously using AASHTO 2012, whereas the end point was that corresponding to the maximum achieved lateral strength of the considered specimen (i.e., at a lateral load of V_P and the corresponding lateral displacement δ_{P1}, see Fig. 2). By defining the post-yield stiffness using the aforementioned start and end points, the curvature in the hardening zone of the load-displacement curves was idealized to a straight line. The second measure was the column displacement ductility, corresponding to the end point of the hardening zone (i.e., $\mu_{P1}=\delta_{P1}/\delta_{Py}$). The two indices were calculated for all specimens and are summarized in Table 5. A detailed explanation concerning the efficiency of the proposed FSRC column design to achieve the desired level of lateral strength (the strength of column CS-4%=67 kN) as well as the effect of the investigated parameters on the post-yield stiffness behavior is as follows:

Fig. 10.a and Table 5 illustrate that control specimen CS-2% continuously increased in lateral strength with the increase in the applied displacement up to a ductility of 5.3 (i.e., μ_{P1}=5.3). The achieved post-yield stiffness ratio corresponding to this final ductility of the hardening zone was 7.8%. Through wrapping the plastic hinge zone with an FRP jacket, as in column CS-2%-J, the column showed an ability to receive a greater lateral load up to μ_{P1} of 9.0, but the post-yield stiffness ratio decreased to 6.6%. A substantial decrease in the column post-yield stiffness ratio of approximately 35% was observed when increasing the amount of steel reinforcement, as in column CS-4%. In contrast, a significant increase in the post-yield stiffness ratio was observed when adding FRP bars, as shown in Fig. 10. Fig. 10.b illustrates that column CSF-2.8%-IS-D10 had a value of k more than twice that of column CS-2%, although the two columns share nearly the same value of μ_{P1}. Changing the location of the FRP bars from the place of the steel fibers (column CSF-2.8%-IS-D10-J) to outside the steel stirrups (in the concrete covers, such as in column CSF-2.8%-ES-D10-J) resulted in a 30% increase in the value of μ_{P1} and a 17% decrease in the value of k, as shown in Fig. 10.c. Furthermore, by adding cross ribs to the surface of the FRP bars, as in column CSF-2.8%-IR-D10-J, the value of k decreased from 17.3% to 12%, although μ_{P1} shifted from 5.8 to 11.3 (see Fig. 10.d). This gives a high responsibility to the surface texture of the FRP bars to control the length of the hardening zone. Finally, the post-yield stiffness represented by the two indices could be increased by using FRP bars with smaller cross-sectional areas. For instance, columns CSF-2.8%-ES-D10-J and CSF-2.8%-ES-D8-J, with the same FRP-to-steel stiffness ratio, had similar values of k, whereas μ_{P1} shifted from 7.7 to 10.4 when decreasing the diameter to 8 mm. This confirmed the previous observation regarding the

ability of the bond conditions of FRP to concrete to control the ductility at the end point of the achieved post-yield stiffness. The previous discussion demonstrated that by adding FRP bars with a good bonding condition to concrete (8-mm-diameter bars or rough bars), the column could achieve the demanded lateral strength at high ductility levels through a stable post-yield stiffness. Compared with these cases, using FRP bars with a weaker bond to concrete resulted in an unfavorable ductility and lateral strength at the end of the post-yield stiffness; however, it results in a larger post-yield stiffness ratio.

Column Ductility

In performance-based seismic design philosophies of reinforced concrete structures, the determination of the deformation capacity of the concrete columns, which are the main earthquake-resisting elements, is of paramount importance. When a structure's earthquake-resistant elements are sufficiently ductile, the structure can undergo large deformations before failure. This is beneficial to provide warning and give sufficient time for taking preventive measures and carrying out suitable repairs to the structure, which can reduce loss of life. Aside from the displacement ductility corresponding to the end point of the post-yield stiffness, as explained in the previous section, three other indices were also used in this study to evaluate the ductility behavior and investigate the effect of the tested parameters. The first is the peak strength stability factor, which measures the ability of a structure to undergo large displacements after achieving the peak lateral strength and before entering the degradation zone {i.e., $SI=(\delta_{P2}-\delta_{P1})/\delta_y$}. The second is the degradation stiffness factor, which defines the ability of a structure to reach its ultimate load through a gradual degradation path {i.e., $K_4=(V_u-V_P)/(\delta u-\delta_{P2}$}. Through this definition, a smaller value of this index indicates a stable, smooth degradation behavior and vice versa. The last ductility measure is the displacement ductility factor at the ultimate lateral strength (μ_u=δ_u /δ_y). Referring to the proposed mechanical model (Fig. 2), Table 5 summarizes the ductility indices for all tested columns.

For the control specimen, after reaching its peak lateral load at a μ_{P1} of 5.3, it achieved a stability index of SI=3.5. This means that the column maintained its peak lateral strength up to a displacement ductility of 8.8 before entering the degradation zone. Following the stability zone, the column reached its ultimate strength at an ultimate displacement ductility, μ_{uC}, of 10.3 through a degradation stiffness factor, K_{4C}, of 0.86.

A significant enhancement in the column ductility could be achieved by wrapping the plastic hinge zone of the steel RC column with an FRP jacket. Although no clear stability zone was formed in column CS-2%-J {i.e., $\mu_{P1} \cong (\mu_{P1} + SI)$ of column CS-2%}, the column fulfilled its ultimate strength (i.e., V_u=0.8V_P) at a displacement ductility of 14.7 (i.e., μ_u=1.43 μ_{uC}) through a degradation factor of 0.27 (i.e., K_4=0.3K_{4C}). In the absence of the FRP jacket, no pronounced enhancement in the ductility indices could be achieved by adding internal smooth FRP bars to the longitudinal reinforcement. Moreover, the weak bond between the FRP bars and surrounding concrete resulted in a relatively sharp degradation curve before reaching the ultimate strength. For instance, the ductility indices SI, $K4$, and μ_u of specimen CSF-2.8%-IS-D10 were 0.97, 1.3, and 0.96 times the corresponding values of specimen CS-2%, respectively. Reviewing the ductility indices of specimens CSF-2.8%-IS-D10 -J (which had smooth FRP bars) and CSF-2.8%-IR-D10-J (which had roughened FRP bars) indicated that the ductility behaviors of the two columns were quite different. Whereas column CSF-2.8%-IS-D10 -J had ductility indices SI, $K4$, and μ_u of 2.1, 1.4, and 9.9, respectively, the corresponding values of column CSF-2.8%-IR-D10-J were 0, 4.14, and 12.3, respectively. This indicates the benefit of roughening the FRP bars to enhance the ultimate ductility of the column (i.e., a 25% increase in μ_u); however, the column suddenly failed upon reaching its peak strength as a result of the FRP rupture. Regarding the effect of the location of the FRP bars on the ductility measurements, the results showed that placing the FRP bars in the concrete covers instead of in the concrete core caused the column to begin to degrade once it achieved its peak strength, without showing stability under the peak load. Moreover, the column could reach its ultimate strength at a greater displacement ductility through a smoother degradation manner. This was clearly observed in the behavior of column CSF-2.8%-ES-D10-J compared to column CSF-2.8%-IS-D10-J, where the ductility indices *K4* and μ_u of column CSF-2.8%-ES-D10-J were 0.5 and 1.4 times those of column CSF-2.8%-IS-D10-J, respectively. The reason for this might be attributed to the increase in the accumulated stresses in the FRP bars when they were installed at a larger effective depth, which in turn causes an increase in the bond stresses between the FRP bars and concrete. Reinforcing the column with 8-mm-diameter FRP bars (column CSF-2.8%-ES-D8-J) caused sudden drops in the lateral strength, similar to the case in the specimen reinforced with roughened FRP bars (column CSF-2.8%-IR-D10-J). However, the degradation curve was gradual as a result of using 3- to 8-mm-diameter bars that ruptured at two different drift levels. Whereas columns CSF-2.8%-ES-D8-J and CSF-2.8%-ES-D10-J share the same ultimate ductility factor, the degradation stiffness factor, *K4*, of column CSF-2.8%-ES-D8-J was nearly three times that of column CSF-2.8%-ES-D10-J. Thus, more experimental investigations on the effect of the bar surface texture (bond conditions) on the ductility indices, particularly the degradation behavior of columns reinforced with steel and FRP bars, are required.

Residual Displacement

To evaluate the behavior of the proposed RC bridge columns after an earthquake, the residual displacement index, which measures the degree of permanent displacement (the displacement of the zero-crossing at unloading on the hysteresis loop from the maximum displacement), was used in this study as an indicator to fully quantify the performance level under seismic loading. Thus, the drift ratio versus normalized residual displacement of all tested columns was drawn as shown in Fig. 11. The normalized residual displacement was defined as the ratio of the residual displacement of each column at a drift level to that of the control column at the same drift level (i.e., $r=\delta_r/\delta_{rC}$). As the value of r for a column decreases, the column becomes more recoverable and reparable. Fig. 11 illustrates that although the value of r up to a drift of 1.7% (onset of FRP participation) was less than one for all columns, no clear stable trend could be observed. Starting from this drift ratio, a stable trend for the value of r could be observed. As expected, wrapping the plastic hinge region using an FRP jacket, as in column CS-2%-J, could not control the residual displacement of the column, where the value of r ranged from 0.95 to 1.02 up to a drift of 8%, at which the control column failed. By contrast, reinforcing the columns with FRP bars clearly decreased the residual displacement. For instance, the average value of the normalized residual displacement of columns CSF-2.8%-IS-D10, CSF-2.8%-IS-D10-J, and CSF-2.8%-ES-D10-J, reinforced with FRP bars having smooth surface textures, was approximately 0.8. The columns maintained this normalized value up to a drift level just before entering the degradation zone of each column as a result of bond failure. Following this drift level, the FRP bars could not continue controlling the residual displacement until the end of the tests. In contrast, the impact on the residual displacement became more considerable when enhancing the bond between the FRP bars and surrounding concrete. This trend can be observed in column CSF-2.8%-IR-D10-J (which had FRP bars with a rough texture) and column CSF-2.8%-ES-D8-J (which had FRP bars with a smaller diameter), where both columns had an average value of r=0.7. The columns continued controlling the residual displacement with nearly the same value of r until the FRP bars ruptured, at which the FRP bars lost their role in controlling the column performance. As a concluding remark, among all of the tested columns, CSF-2.8%-ES-D8-J had the best seismic performance in terms of the smallest residual displacement. This performance was caused by the high post-yield stiffness, in the plastic zone.

Dissipated Energy and Damping Ratio

Ductile structures should be able to dissipate significant energy during major seismic events before failure. In recent decades, two indices have been defined to describe the ability of a structure to dissipate earthquake energy and hence survive major seismic events. The first index is the cumulative dissipated energy, which is computed by summing up the areas enclosed by the hysteretic loops in the lateral load-displacement relationships of the structure up to failure. The other index is the viscous damping ratio, which reflects the damage level attained during inelastic excursions. In this section, the cumulative dissipated energy, E, for all tested specimens was recorded and plotted for each drift level to further evaluate the effectiveness of the proposed reinforcement and investigate the effect of each tested parameter, as shown in Fig. 12. In the same manner, the damping ratio versus the displacement ductility were calculated and plotted for all specimens, as shown in Fig. 13.

Dissipated Energy

After calculating the energy dissipated by each loading cycle, the cumulative dissipated energy up to each drift level was determined, and the effect of each parameter was addressed, as shown in Fig. 12. Fig. 12 illustrates that the investigated parameters had only a minor impact on the cumulative dissipated energy. All columns shared almost the same cumulative dissipated energy of approximately 27 kN.m up to a drift of 6%. The effects of the investigated parameters were apparent beyond this drift level. After a drift of 7%, no pronounced increase in the cumulated dissipated energy was observed in the control specimen, CS-2%, as a result of the cover spalling and bar buckling that caused the failure of the specimen. By wrapping the plastic hinge with an FRP jacket, as in column CS-2%-J, the column continued dissipating more energy up to a drift of 9.4%, at which E was equal to $1.7E_C$, where E_C is the total cumulative dissipated energy of the control specimen up to failure. Then, the rate of increase was small due to the FRP sheet bulging, which led to the failure of that column. Fig. 12 also illustrates that although adding FRP bars to the steel reinforcement caused a substantial increase in the post-yield stiffness ratio, the column was able to dissipate more energy up to failure. The aforementioned observations suggest that the efficiency of reinforcing the columns with both steel and FRP bars on the amount of dissipated energy may be controlled by other variables. Thus, further investigations are still needed to determine the best configuration and best surface treatment to optimize the dissipated energy.

Equivalent Viscous Damping Ratio

The equivalent viscous damping, ζ_i, for the first cycle of all loading sets was calculated using equation 2 (Elmenshawi and Brown 2010).

$$\zeta_i = E_i/(4\pi E_{si}) \qquad (2)$$

where E_i and E_{si} refer to the dissipated energy and elastic energy in the cycle i, respectively.

Fig. 13 shows the effect of each testing parameter on the relationship between the displacement ductility, μ, and calculated damping ratio, ζ%. Fig. 13 illustrates that up to a displacement ductility of two, only slight differences in the damping ratio, ζ, were observed in all columns, where at this ductility, the average value of ζ was approximately 12%. There was a small decrease in the ζ for specimen CS-2%-J compared to the control specimen CS-2%, particularly after a displacement ductility of 9, at which the concrete cover of column CS-2% spalled, as shown in Fig. 13.a. A comparison of the results of column CSF-2.8%-IS-D10 with the control column (see Fig. 13.b) indicates that the decrease in ζ was more evident up to a displacement ductility of 9, at which both the columns started to degrade; the average loss in the value of ζ in this column was approximately 20%. Moreover, the comparison of the results of columns CSF-2.8%-IS-D10-J and CSF-2.8%-IR-D10-J with that of column CS-2%-J (see Fig. 13.d) illustrates that while reinforcing the column with internal smooth FRP bars resulted in a minor decrease in ζ up to the appearance of bond slip failure at a ductility of 8%, this decrease was more evident when using roughened FRP bars (i.e., 33% decrease). For both columns, the value of ζ approaching the failure was closer to that of specimen CS-2%-J. The average value of ζ for I-S-10-J and I-R-10-J up to failure was nearly 86% and 75% of that of specimen C-J, respectively. By placing the FRP bars externally instead of internally, as in column CSF-2.8%-ES-D10-J, the value of ζ became lower, where the average value of ζ for specimen CSF-2.8%-ES-D10-J was almost 88% of that of specimen CSF-2.8%-IS-D10-J (see Fig. 13.c). Finally, Fig. 13.e illustrates that using FRP bars with 8-mm-diameter caused a greater decrease in the value of ζ compared with the counterpart 10-mm-diameter BFRP bars. In other words, the decrease in the damping ratio was more pronounced when using FRP bars with a stronger bond to the surrounding concrete. This discussion demonstrates that although using FRP bars as the main reinforcement helped the column achieve higher levels of post-yield stiffness without causing any loss in the column ductility and dissipated energy, the decrease in the damping ratio could be acceptable to achieve the aim of damage-controlling structures.

Which FSRC Column Could Successfully Achieve a Ductile-Recoverable Performance?

In the light of the targeted structural performance of the proposed FRP-steel RC structure, two columns could achieve the demanded ductile-recoverable performance. The first is CSF-2.8%-

IR-D10-J (which had FRP bars with rough textures and was wrapped with an FRP jacket), and the second is column CSF-2.8%-ES-D8-J (which had FRP bars with a smaller diameter and was wrapped with an FRP jacket). Both these columns had an average value for the post-yield stiffness ratio of 12.6%, an average displacement ductility before load degradation of 10.85, an average ultimate ductility of 12.85, and an average residual displacement of 0.7 times that of the steel RC columns. This performance was caused by the good bonding between the FRP bars and surrounding concrete.

Summary and Conclusions

In this study, an FRP-steel RC structure was proposed as a high-seismic-performance structure. The mechanical model describing the performance of this structure during and after earthquake actions was first discussed. Experimental tests on the effect of constant axial load and several cyclic loadings were conducted on seven RC bridge columns, where two columns simulated the performance of steel RC bridge columns and the others showed the response of the proposed BFRP-steel RC columns. The roles of several bond-based parameters, such as the diameter of the FRP bars, texture of the FRP bars, location of the added FRP bars, and external confinement using an FRP jacket, were examined through the experimental program. The following conclusions could be drawn from this study:

1) With a proper design of the proposed FRP-steel reinforcement for concrete bridge columns, it is possible to withstand strong earthquakes with a targeted ductility by ensuring the existence of a stable post-yield stiffness without a considerable increase in the elastic stiffness. Moreover, the post-earthquake reparability can be enhanced by mitigating the residual displacement;

2) Both the surface texture configuration and the diameter of the cross section of the FRP bars significantly influence the seismic performance and failure mode of FRP-steel RC bridge columns. Using 10-mm-diameter BFRP bars with a rough surface texture or 8-mm-diameter bars with small indentations resulted in a rupture of the BFRP bars that was accompanied by a sharp brittle failure after achieving a high strength level with reasonable ductility. Using BFRP bars with a smooth surface texture of 10-mm diameter caused a lower and more stable peak strength at a smaller ductility with a smoother degradation
3) Changing the location of BFRP bars in the column cross section with respect to the steel reinforcement caused only a marginal change in the column post-yield stiffness ratio and column ductility before strength degradation. However, compared with adding FRP bars internally in the same fibers as the steel bars, placing them in the concrete cover caused a considerable increase in the elastic stiffness and eliminated the stability plateau at the peak strength before strength degradation.
4) External confinement of the steel RC column with BFRP sheets caused a slight increase in the column strength with a stable degradation stiffness and a substantial increase in the displacement ductility before failure.
5) Although adding BFRP bars caused a remarkable enhancement in the plastic deformation, no significant decrease in the damping ratio could be observed. Moreover, a comparable cumulative dissipated energy was evident.
6) Increasing the column strength to withstand a strong earthquake using additional steel reinforcement greatly increased the column elastic stiffness and decreased the column post-yield stiffness ratio. In contrast, by adding FRP reinforcement, nearly the same level of lateral

strength could be achieved with a significant increase in the column post-yield stiffness ratio and without any substantial increase in the elastic stiffness.

7) Future research should be directed toward providing a better understanding of the behavior of such FRP-steel reinforcements with an emphasis on the bond condition's effect on the post-peak stability, residual displacement, and degradation stiffness. Other design parameters, including the FRP-to-steel stiffness ratio and transverse FRP reinforcement ratio, should also be examined.

References

AASHTO. (2012). AASHTO LRFD Bridge Design Specifications, American Association of State Highway and Transportation Officials, Washington, D.C.

Christopoulos, C., Pampanin, S., and Priestley, M. J. (2003). "Performance-based seismic response of frame structures including residual deformations. Part I: Single-degree of freedom systems." *J. Earthquake Eng.*, 7(1), 97–118.

Christopoulos, C., and Pampanin, S. (2004). "Towards performance-based seismic design of MDOF structures with explicit consideration of residual deformations." *ISET Journal of Earthquake Technology*, 41(1), 53–73.

Dhakal, R. P., and Maekawa, K. (2002). "Reinforcement stability and fracture of cover concrete in reinforced concrete members." *J. Struct. Eng.*, 128(10), 1253-1262.

Elmenshawi, A., and Brown, T. (2010). "Hysteretic energy and damping capacity of flexural elements constructed with different concrete strengths." *J. Eng. Struc.*, 32(1), 297-305.

Fahmy, M. F. M., Wu, Z. S., and Wu, G. (2009). "Seismic performance assessment of damage controlled FRP-retrofitted RC bridge columns using residual deformations." *J. Compos. Constr.*, ASCE, 13(6):498-513.

Fahmy, M. F. M., Wu, Z. S., and Wu, G., (2010) “Post-earthquake recoverability of existing RC bridge piers retrofitted with FRP composites.” *Constr. and Building Mater.*, 24(6), 980-998.

Iemura, H., Takahashi, Y., and Sogabe, N. (2006). “Two-level seismic design method using post-yield stiffness and its application to unbonded bar reinforced concrete piers.” *Struct. Eng./Earthquake Eng.*, 23(1), 109s–116s.

Ikeda, S., Nonaka, S., Hirose, S., and Yamagushi, T. (2002) “Seismic performance of concrete piers prestressed in the critical section.” In: *Proceedings of the First FIB Congress*, Osaka, Japan, 47-48.

Kawashima, K. (2000). “Seismic design and retrofit of bridges.” *Bull. New Zeal. Natl. Soc. Earthquake Eng.*, 33(3), 265–285.

Kawashima, K., MacRae, G. A., Hoshikuma, J., and Nagaya, K. (1998). “Residual displacement response spectrum.” *J. Struct. Eng.*, 124(5), 523–530.

Mazzoni, S., McKenne, F., Scott, M. H., Fenves, G. L. et al. Open system for earthquake engineering simulation user manual version 2.4.5. Berkeley (CA): Pacific Earthquake Engineering Center, University of California. http:// http://opensees.berkeley.edu/

Palmieri, A., Matthys, S., and Tierens, M. (2009). “Basalt fibers: mechanical properties and applications for concrete structures.” *Taylor & Francis Group*, London, UK, 165-169.

Pettinga, D., Christopoulos, C., Pampanin, S., and Priestley, N. (2007). “Effectiveness of simple approaches in mitigating residual deformations in buildings.” *Earthquake Eng. Struct. Dyn.*, 36(12), 1763–1783.

Priestley, M., Seible, F., and Calvi, G. M. (1996). *Seismic design and retrofit of bridges*, Wiley, New York.

Saiidi, M. S., O'Brien, M., and Zadeh, M. S. (2009). "Cyclic response of concrete bridge columns using superelastic nitinol and bendable concrete." *ACI Struct J.*, 106(1), 69-77.

Sakai, J., Jeong, H., and Mahin, S.a. (2006) "Reinforced concrete bridge columns that re-center following earthquakes." *In: Proceedings of the 8th National conference on Earthquake Engineering*, San Francisco, CA, paper no. 1421.

Sim, J., Park, C., and Moon, D.Y. (2005). "Characteristic of basalt fiber as a strengthening material for concrete structures." *Composites: Part B Eng.*, 36(6), 504-512.

Wehbe, N. I., Saiidi, M. S., and Sanders, D. H (1999). "Seismic Performance of Rectangular Bridge Columns with Moderate Confinement." *ACI Struct J*., 96(2), 248-258

Wu, Z. S., Fahmy, M. F. M., and Wu, G. (2009). "Safety enhancement of urban structures with structural recoverability and controllability." *J. Earthquake Tsunami*, 3(3), 143–174.

Wu, G.,Wu, Z. S., Luo, Y. B., Sun, Z. Y., and Hu, X. Q. (2010). "Mechanical properties of steel-FRP composite bar under uniaxial and cyclic tensile loads." *J. Mater. Civ. Eng.*, 22(10), 1056–1066.

Wu, Z., Wang, X., Iwashita, K., Sasaki, T., and Hamaguchi, Y. (2010). "Tensile fatigue behavior of FRP and hybrid FRP sheets." *Composites: Part B Eng.*, 41(5), 396-402.

Zatar, W. A., and Mutsuyoshi, H. (2002). "Residual displacement of concrete bridge piers subjected to near field earthquakes." *ACI Struc. J.*, 99(6), 740-749.

Figure captions

Fig. 1. Schematic model of: a) proposed FSRC structure and b) conventional SRC structure (SRC1 and SRC2).

Fig. 2. Targeted idealized load deformation behavior of the proposed FRP-steel RC column versus steel RC columns, based on the damage-controlled model for existing RC structures (Fahmy et al. 2009).

Fig. 3. Typical test unit (dimensions are in mm) and instrumentation of a test specimen

Fig. 4. Cross sections and reinforcement details of specimens (dimensions are in mm).

Fig. 5. Configuration of the surface texture of FRP bars.

Fig. 6. Typical arrangement of strain gauges.

Fig. 7. Load versus drift ratio curves of column specimens.

Fig. 8. State of the column specimens at failure.

Fig. 9. Load versus BFRP bar strain of FSRC columns.

Fig. 10. Effect of the investigated parameters on the average envelope response.

Fig. 11. Normalized residual displacement versus lateral drift ratios of the tested columns.

Fig. 12. Effect of all investigated parameters on the cumulative dissipated energy.

Fig. 13. Effect of all investigated parameters on the damping ratio.

Table 1. Mechanical properties of steel and FRP materials

Material type	Elastic modulus E (GPa)	Yield stress f_y (MPa)	Tensile strength f_u (MPa)
Longitudinal steel bars	200	375	560
Transverse steel bars	200	400	625
10 mm diameter BFRP bars	48.1	-------	1113
8 mm diameter BFRP bars	47.3	-------	1086
BFRP sheet	91	-------	2100

Note: (1) Tensile strengths of the BFRP bars were defined based on the cross-sectional area of each bar. (2) Based on the manufacturer, the basalt fiber content was 60% of the cross-sectional area.

Table 2. Experimental Parameters

Specimen number	$f_{c'}$ (MPa)	Steel reinforcement		BFRP reinforcement			ρ_l %	L_{j1} (mm)
		Main	Transverse	Location	Surface	Components		
CS-2%	27.8	6Φ13	Φ6@50 mm	-----	------	------	2	-----
CS-2%-J	31.4	6Φ13	Φ6@50 mm	-----	------	------	2	300
CSF-2.8%-IS-D10	35.4	6Φ13	Φ6@50 mm	Internal	Smooth	4Φ10	2.8	-----
CSF-2.8%-IS-D10-J	41.2	6Φ13	Φ6@50 mm	Internal	Smooth	4Φ10	2.8	300
CSF-2.8%-IR-D10-J	32.9	6Φ13	Φ6@50 mm	Internal	Roughened	4Φ10	2.8	300
CSF-2.8%-ES-D10	32.7	6Φ13	Φ6@50 mm	External	Smooth	4Φ10	2.8	600
CSF-2.8%-ES-D8	34.5	6Φ13	Φ6@50 mm	External	Smooth	6Φ8	2.8	600

Note: $f_{c'}$ is the actual concrete compressive strength on the day of testing; ρ_l is the total reinforcement ratio of the steel and FRP bars; L_{j1} is the length of the first 0.333-mm-thick FRP jacket above the column base.

Table 3. Positive and negative characteristic values of the hysteretic curves of the tested columns

Specimen number	V_y (kN)	δ_y (mm)	ε_{fy} ($\mu\varepsilon$)	V_P (kN)	δ_{P1} (mm)	δ_{P2} (mm)	V_u (kN)	δ_u (mm)	ε_{fu} ($\mu\varepsilon$)	Failure mode
CS-2%	+26.0	+5.4	-------	+37.3	+30.0	+50.0	+29.8	+58.5	----	Cover spalling and bar buckling
	-26.8	-6.0	-------	-37.8	-30.0	-50.1	-30.2	-59.0	----	
CS-2%-J	+27.2	+5.6	-------	+43.3	+50.0	+50.0	+34.6	+83.2	----	Fracture of steel bars
	-27.6	-5.5	-------	-43.5	-50.0	-50.0	-34.8	-80.0	----	
CSF-2.8%-IS-D10	+30.8	+7.9	+2032	+48.0	+30.0	+59.9	+37.5	+70.1	+10972	Local bond slip of FRP bars
	-27.6	-6.3	-1888	-50.0	-41.3	-59.9	-37.5	-70.1	-13908	
CSF-2.8%-IS-D10-J	+28.1	+5.3	+1748	+56.75	+50	+59.1	+37.5	+70.0	+12283	Local bond slip of FRP bars
	-36.7	-9.6	-2512	-59	-40.0	-58.7	-37.5	-76.9	-13160	
CSF-2.8%-IR-D10-J	+29.4	+6.5	+2019	+60.0	+69.7	+69.7	+37.5	+76.4	----	Rupture of FRP bars
	-28.1	-5.9	-2192	-69.0	-70.1	-70.1	-37.5	-76.4	-16330	
CSF-2.8%-ES-D10-J	+33.2	+5.7	+2292	+61.0	+40.8	+40.8	+37.5	+80.0	----	Local bond slip of FRP bars
	-30.8	-5.8	-1982	-60.0	-48.0	-50.0	-37.5	-80.0	-14152	
CSF-2.8%-ES-D8-J	+32.9	+6.0	+2911	+68.0	+60.0	+60.0	+37.5	+80.0	----	Rupture of FRP bars
	-31.9	-5.6	-2603	-71.0	-60.0	-60.0	-37.5	-74.9	-22272	

Note: the symbols "+" and "-" stand for the characteristic values in the positive and negative loading directions, respectively.

Table 4. Average characteristic values of the hysteretic curves of the tested columns

Specimen number	V_{cr} (kN)	δ_{cr} (mm)	V_y (kN)	δ_y (mm)	ε_{fy} ($\mu\varepsilon$)	V_P (kN)	δ_{P1} (mm)	δ_{P2} (mm)	V_u (kN)	δ_u (mm)	ε_{fu} ($\mu\varepsilon$)
CS-2%	9.2	0.9	26.4	5.7	-------	37.5	30.0	50.1	30.0	58.8	-------
CS-2%-J	9.4	1.0	27.4	5.5	-------	43.4	50.0	50.0	34.7	81.6	-------
CSF-2.8%-IS-D10	10.0	1.3	29.2	7.1	1960	49.0	35.6	59.9	37.5	70.1	12440
CSF-2.8%-IS-D10-J	10.6	1.2	32.4	7.4	2130	57.1	45	58.9	37.5	73.4	12721
CSF-2.8%-IR-D10-J	10.7	1.2	28.8	6.2	2106	64.5	69.9	69.9	37.5	76.4	16330
CSF-2.8%-ES-D10-J	12.6	1.1	32.0	5.8	2137	60.5	44.4	45.4	37.5	80.0	14152
CSF-2.8%-ES-D8-J	12.7	1.0	32.4	5.8	2757	69.5	60.0	60.0	37.5	77.5	22272

Table 5. Ductility and stiffness indices of the investigated columns

Specimen number	Stiffness indices			Ductility indices			
	K_1 (kN/mm)	K_2 (kN/mm)	k (%)	μ_{P1} (mm/mm)	SI (mm/mm)	K_4 (kN/mm)	μ_u (mm/mm)
CS-2%	4.6	0.36	7.8	5.3	3.5	0.86	10.3
CS-2%-J	4.9	0.33	6.6	9.0	0.0	0.27	14.7
CSF-2.8%-IS-D10	4.1	0.69	16.7	5.0	3.4	1.14	9.9
CSF-2.8%-IS-D10-J	4.4	0.76	17.3	5.8	2.1	1.40	9.9
CSF-2.8%-IR-D10-J	4.6	0.56	12.0	11.3	0.0	4.14	12.3
CSF-2.8%-ES-D10-J	5.5	0.80	14.4	7.7	0.0	0.65	13.8
CSF-2.8%-ES-D8-J	5.6	0.73	13.1	10.4	0.0	1.83	13.4
CS-4%	9.6	0.48	5.0	10.0	------	----	10.0

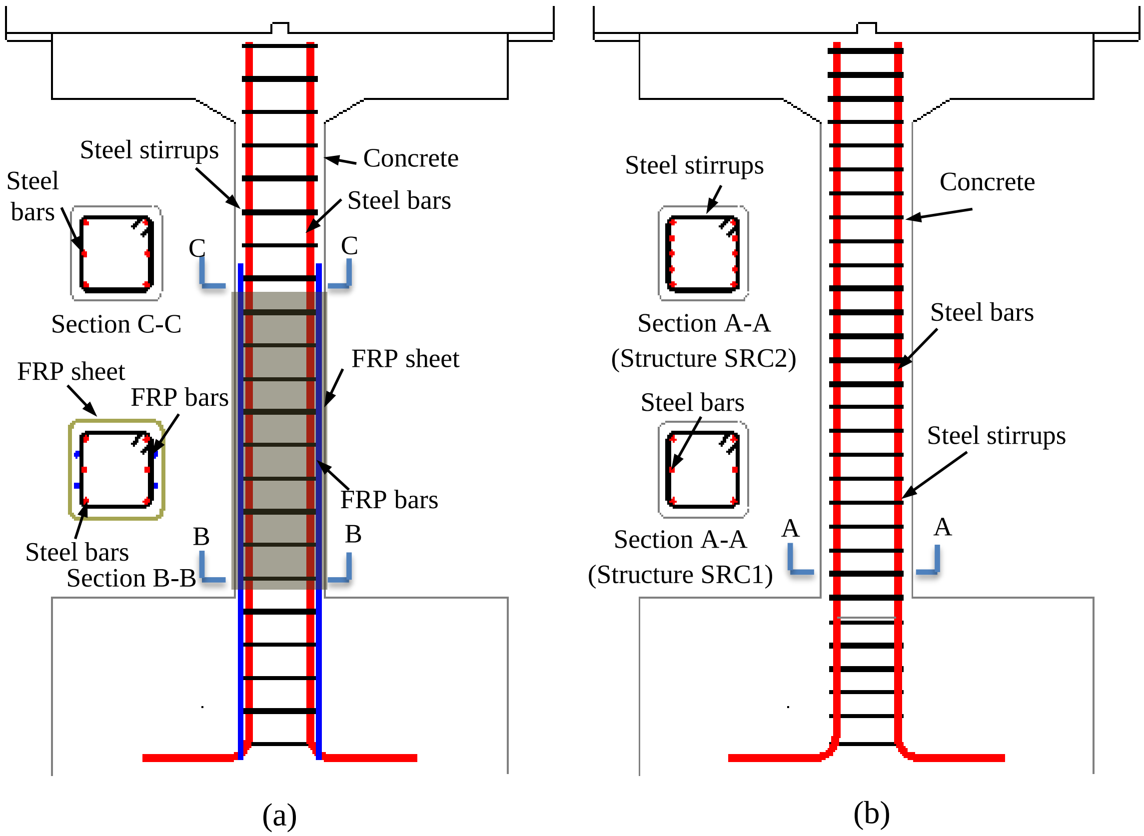

Fig. 1. Schematic model of: a) proposed FSRC structure and b) conventional SRC structure (SRC1 and SRC2)

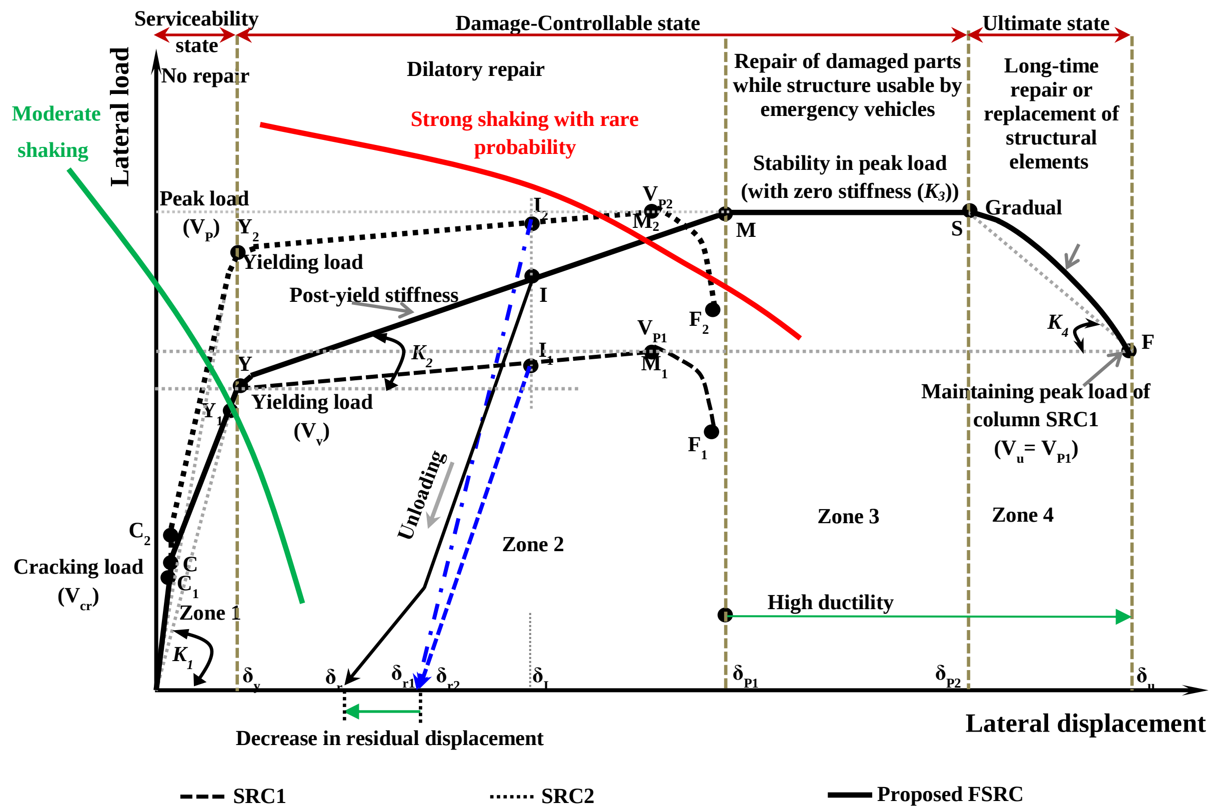

Fig. 2. Targeted idealized load deformation behavior of the proposed FRP-steel RC column versus steel RC columns, based on the damage-controlled model for existing RC structures (Fahmy et al. 2009)

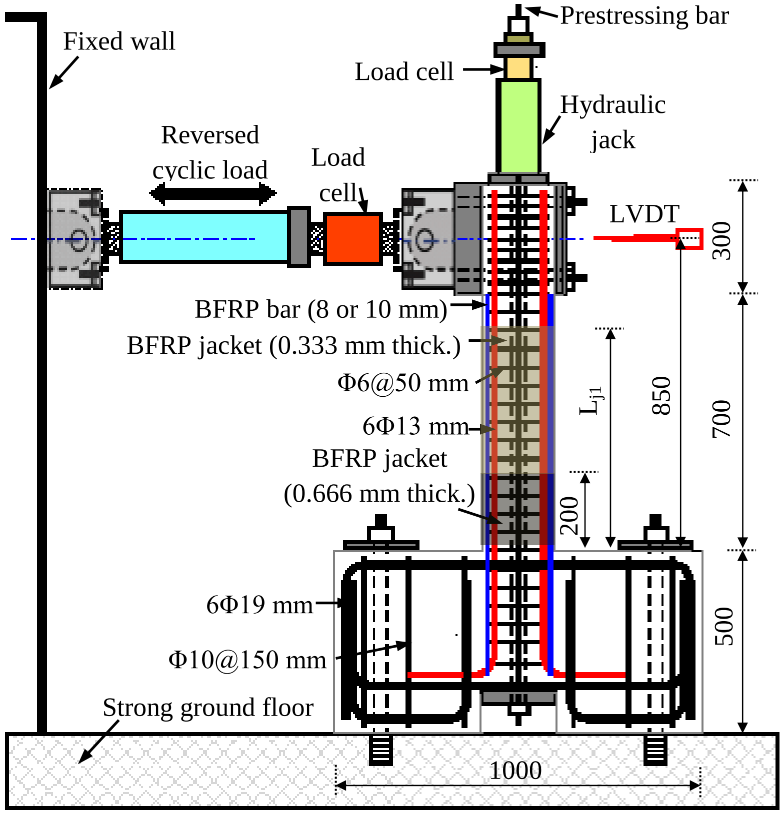

Fig. 3. Typical test unit (dimensions are in mm) and instrumentation of a test specimen

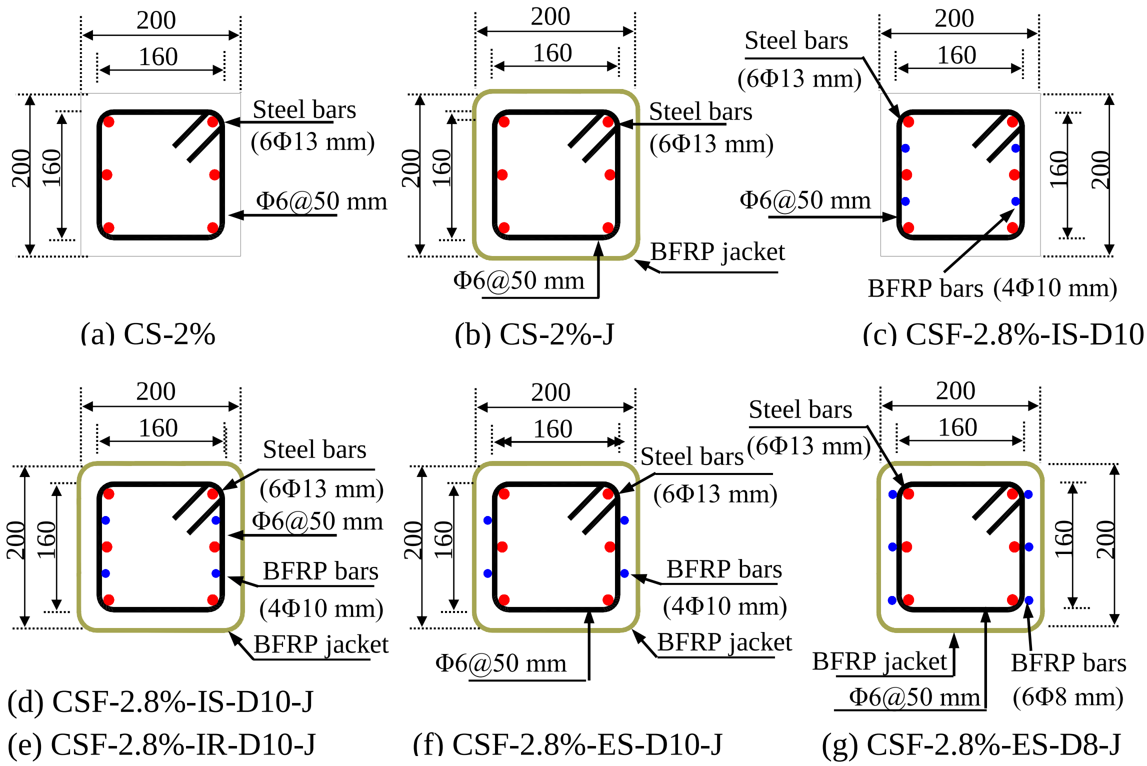

Fig. 4. Cross sections and reinforcement details of specimens (dimensions are in mm)

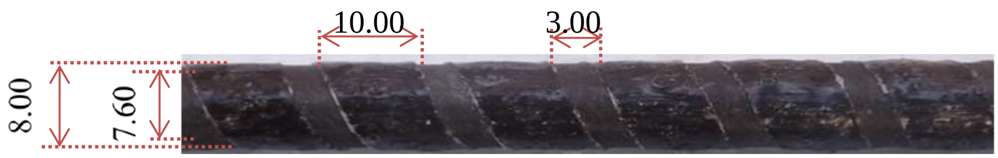

(a) 8-mm-diameter BFRP bar with surface having small indentations (smooth D8)

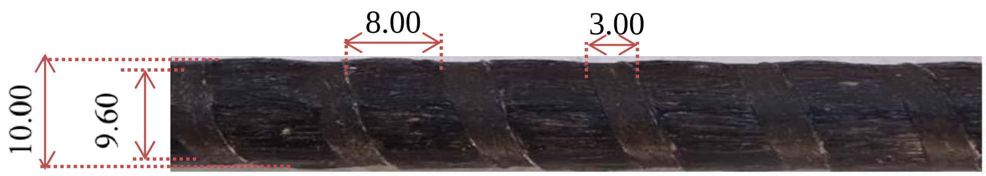

(b) 10-mm-diameter BFRP bar with surface having small indentations (smooth D10)

(c) 10-mm-diameter BFRP bar with cross roughened surface (rough D10 bar)

Fig. 5. Configuration of the surface texture of FRP bars

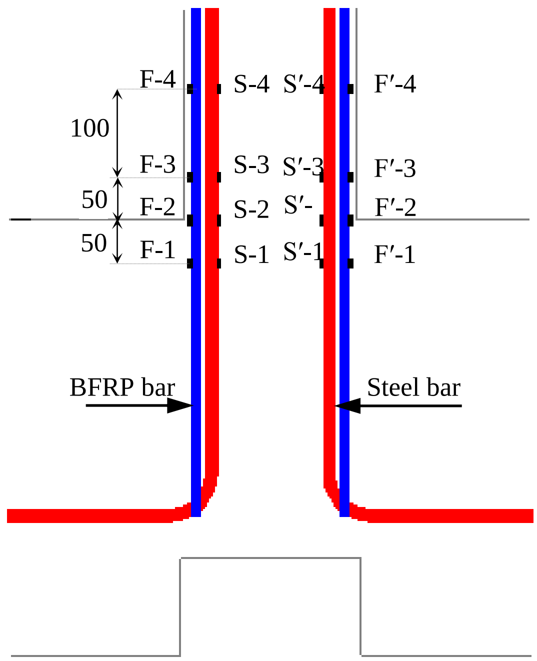

Fig. 6. Typical arrangement of strain gauges

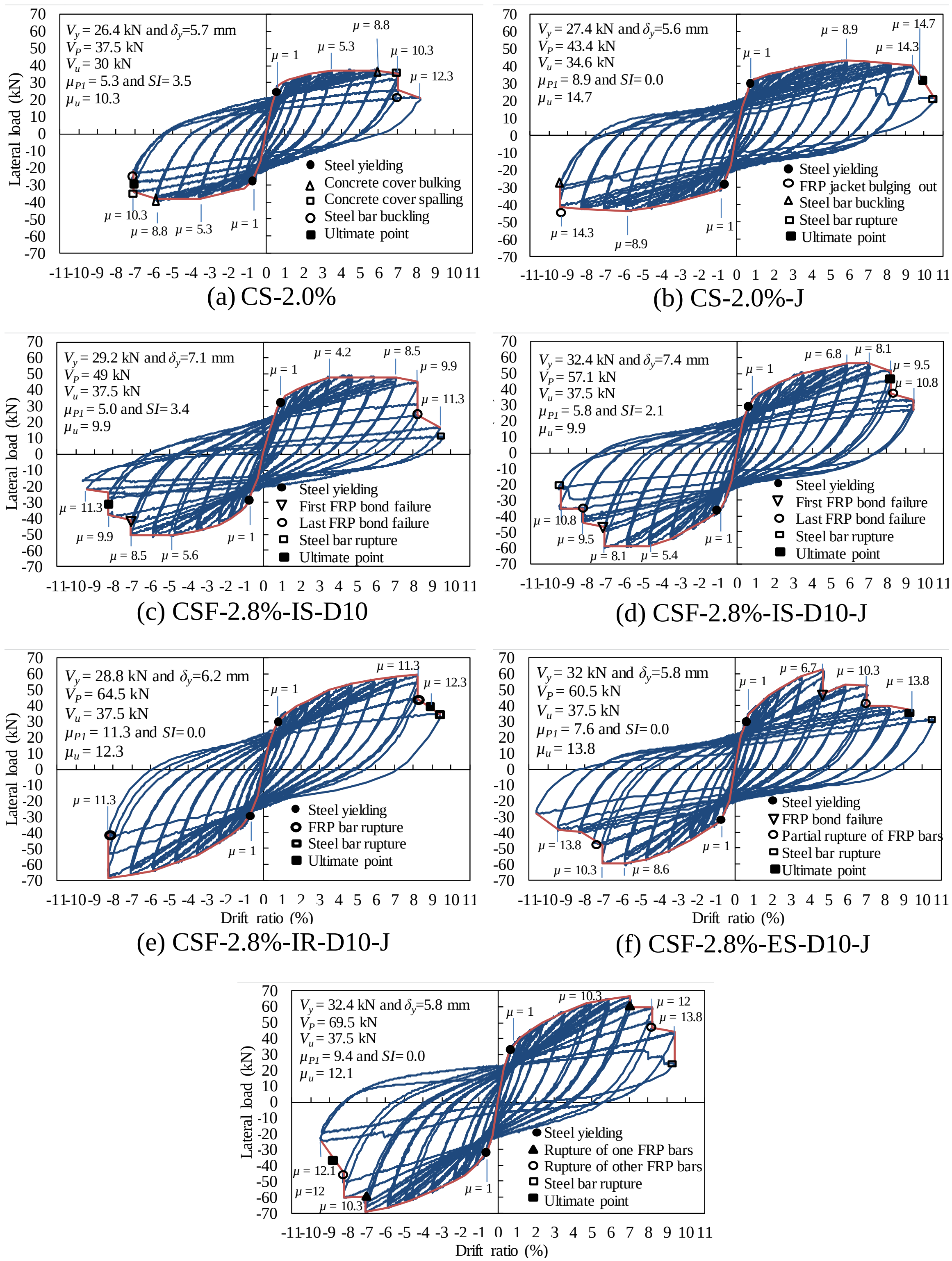

(a) CS-2.0% (b) CS-2.0%-J

(c) CSF-2.8%-IS-D10 (d) CSF-2.8%-IS-D10-J

(e) CSF-2.8%-IR-D10-J (f) CSF-2.8%-ES-D10-J

(g) CSF-2.8%-ES-D8-J

Fig. 7. Load versus drift ratio curves of column specimens

(a) CS-2%

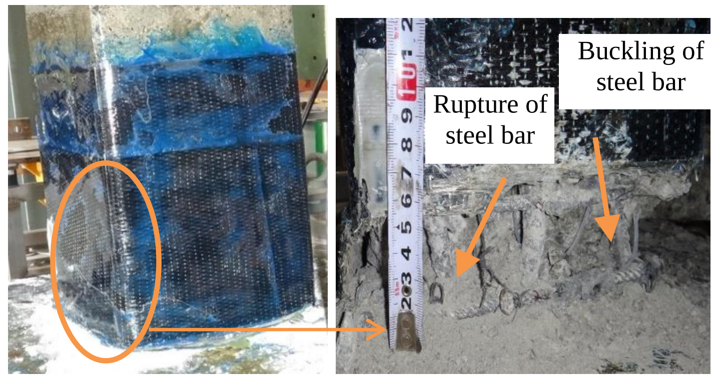

(b) CS-2%-J

(c) CSF-2.8%-IS-D10

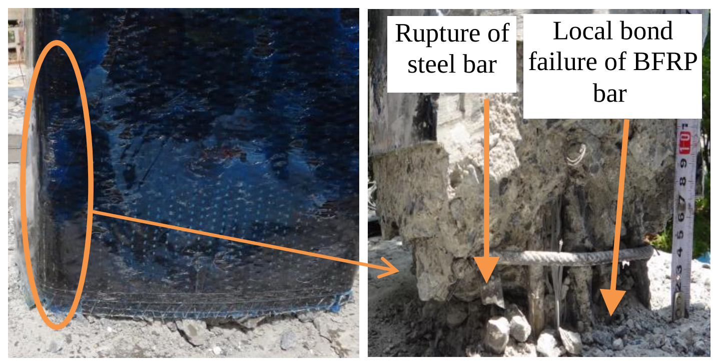

(d) CSF-2.8%-IS-D10-J

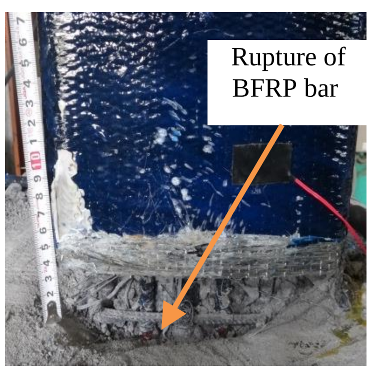

(e) CSF-2.8%-IR-D10-J

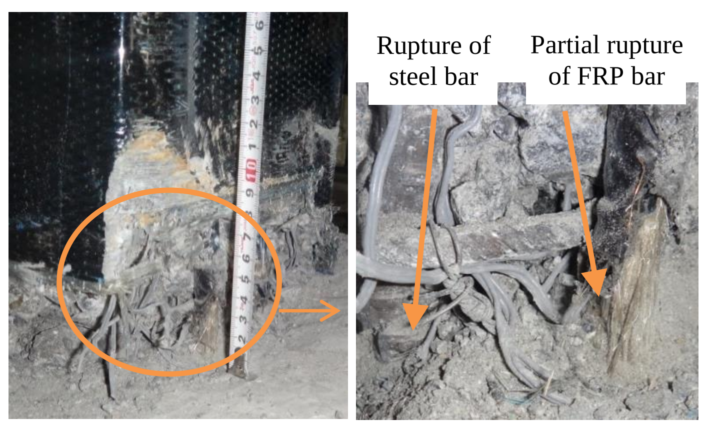

(f) CSF-2.8%-ES-D10-J

(g) CSF-2.8%-ES-D8-J

Fig. 8. State of the column specimens at failure

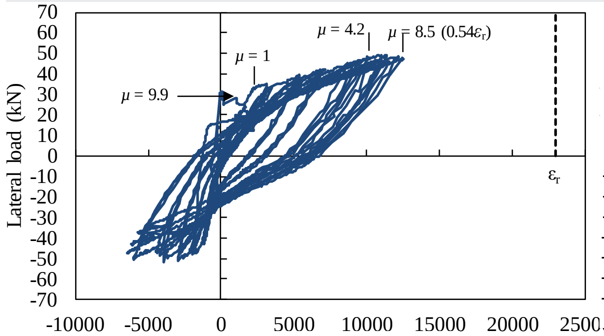

(c) CSF-2.8%-IS-D10
(at 50 mm above column base, F-3)

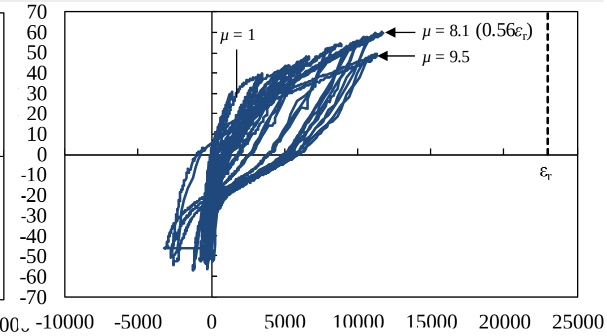

(d) CSF-2.8%-IS-D10-J
(at 50 mm above column base, F-3)

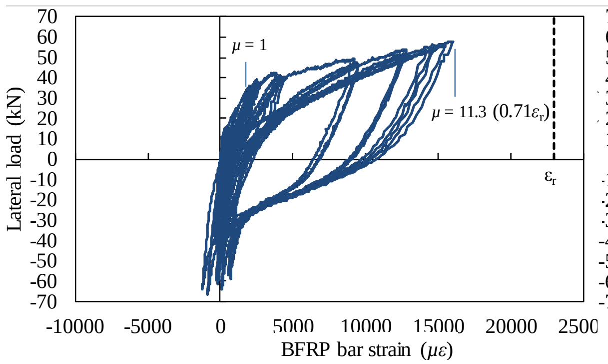

(e) CSF-2.8%-IR-D10-J
(at 150 mm above column base, F-4)

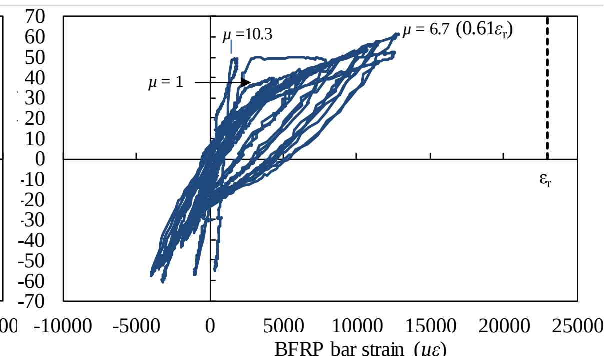

(f) CSF-2.8%-ES-D10-J
(at 50 mm above column base, F-3)

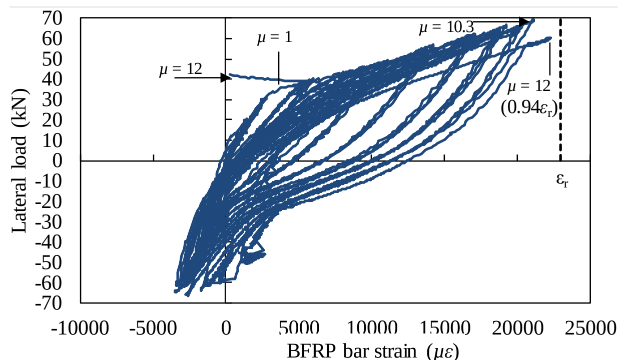

(g) CSF-2.8%-ES-D8-J
(at 50 mm above column base, F-3)

Fig. 9. Load versus BFRP bar strain of FSRC columns

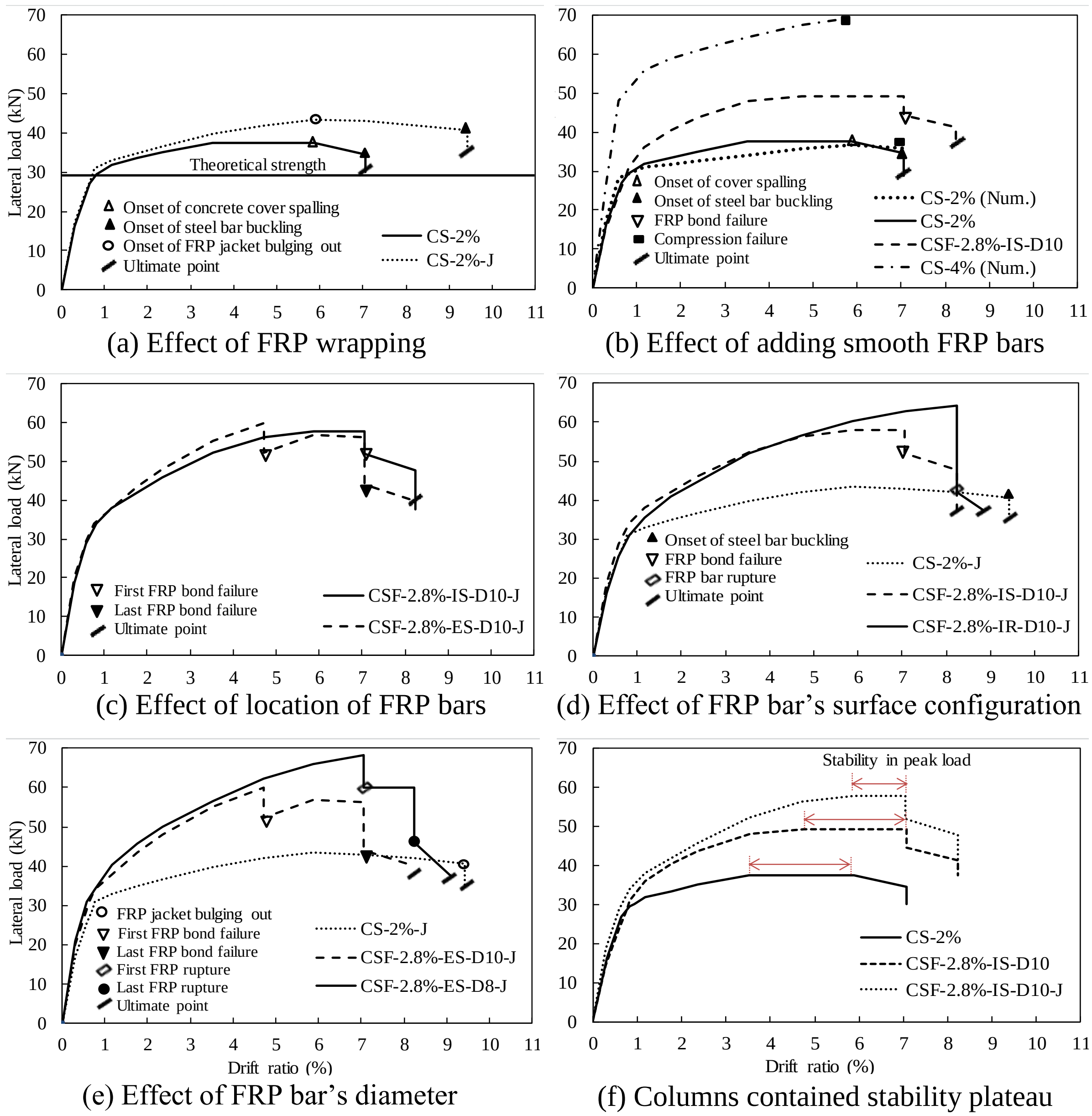

Fig. 10. Effect of the investigated parameters on the average envelope response

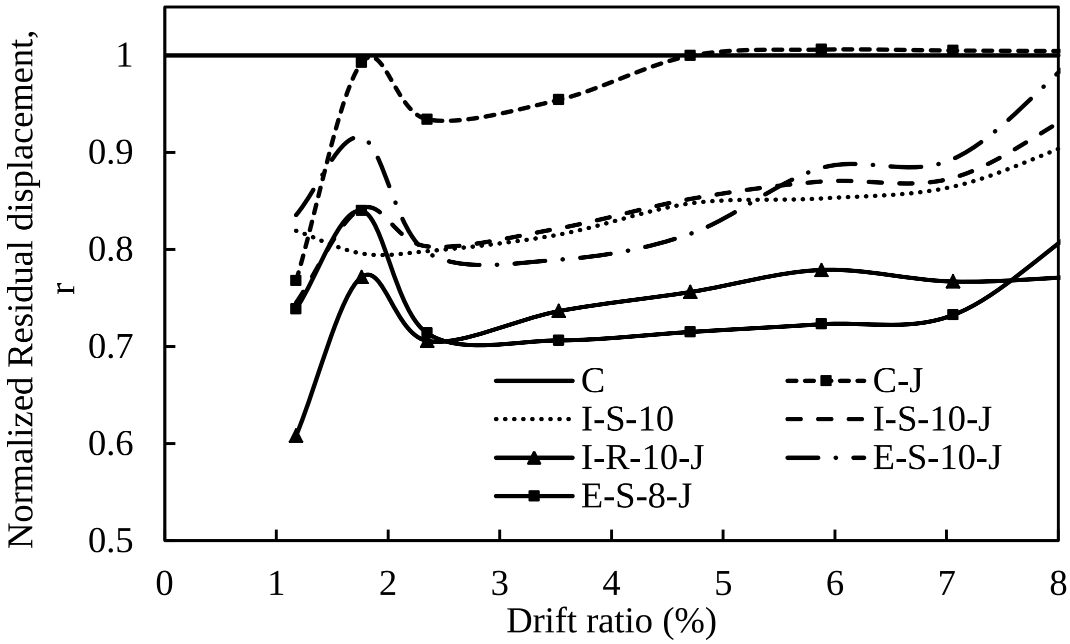

Fig. 11. Normalized residual displacement versus lateral drift ratios of the tested columns

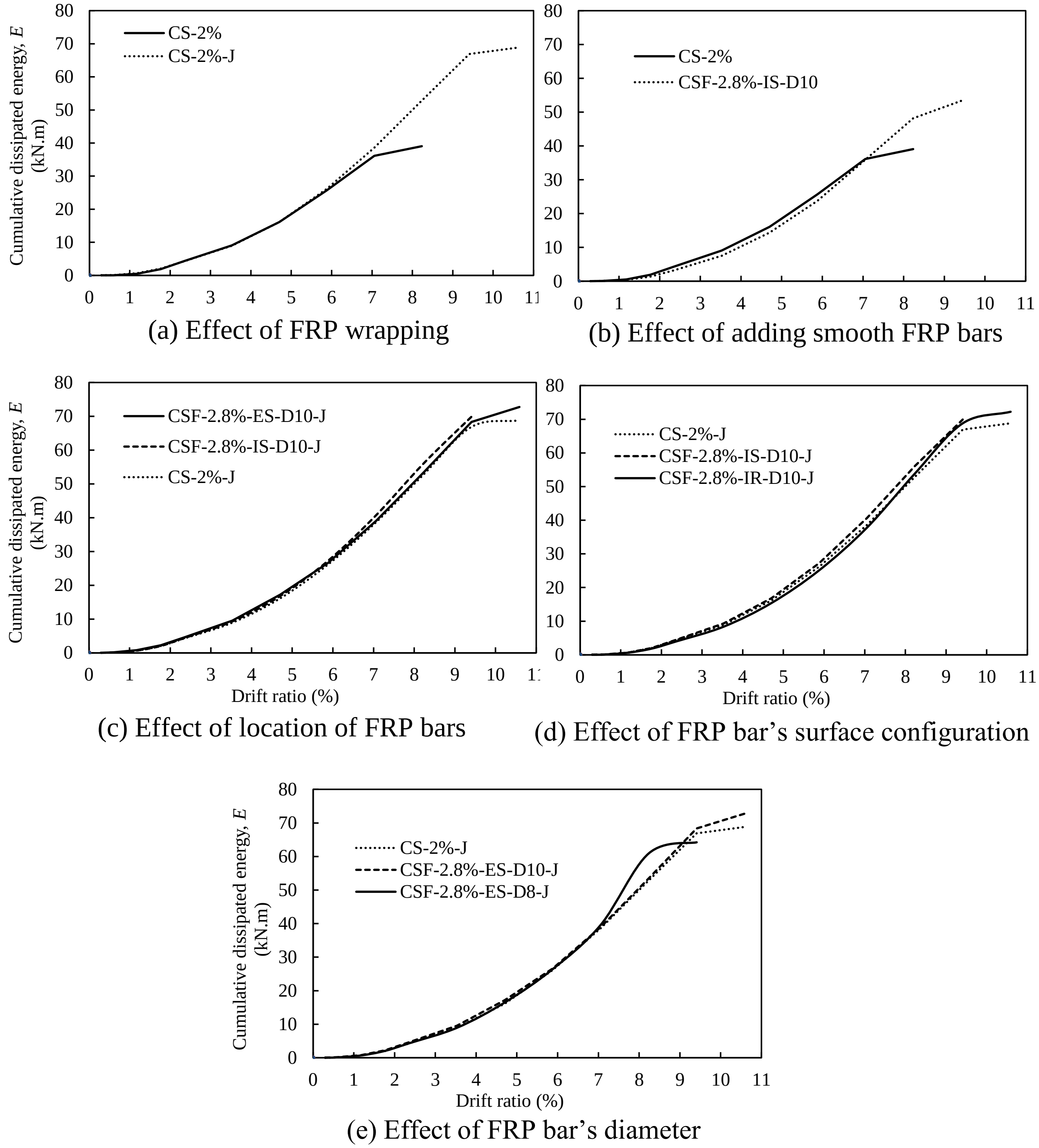

Fig. 12. Effect of all investigated parameters on the cumulative dissipated energy

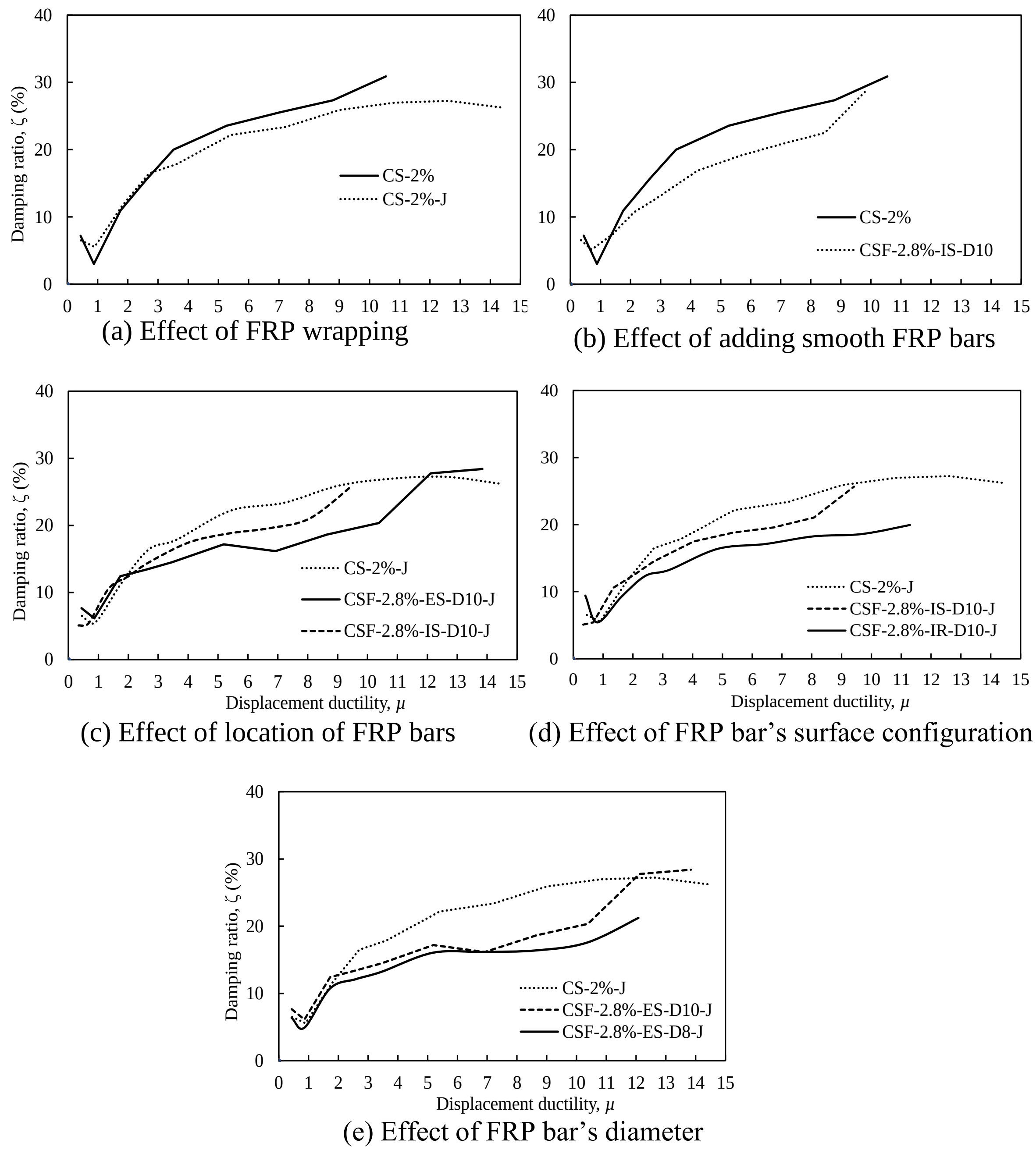

Fig. 13. Effect of all investigated parameters on the damping ratio

PAPER Special Section on Signal Design and Its Applications in Communications

Theoretical Analysis of New PN Code on Optical Wireless Code-Shift-Keying

Yusuke TAKAMARU†a), Sachin RAI†b), *Student Members, and* Hiromasa HABUCHI††c), *Member*

SUMMARY A code shift keying (CSK) using pseudo-noise (PN) codes for optical wireless communications with intensity/modulation and direct detection (IM/DD) is considered. Since CSK has several PN codes, the data transmission rate and the bit error rate (BER) performance can be improved by increasing the number of PN codes. However, the conventional optical PN codes are not suitable for optical CSK with IM/DD because the ratio of the number of PN codes and the code length of PN code, M/L is smaller than $1/\sqrt{L}$. In this paper, an optical CSK with a new PN code, which combines the generalized modified prime sequence code (GMPSC) and Hadamard code is analyzed. The new PN code can achieve $M/L = 1$. Moreover, the BER performance and the data transmission rate of the CSK system with the new PN code are evaluated through theoretical analysis by taking the scintillation, background-noise, avalanche photodiode (APD) noise, thermal noise, and signal dependent noise into account. It is found that the CSK system with the new PN code outperforms the conventional optical CSK system.

key words: *CSK, GMPSC, Hadamard code, PN code, IM/DD, optical wireless communication*

1. Introduction

Optical wireless communications (OWC), which include visible-light communications and intensity-modulation and direct-detection (IM/DD) systems, are of considerable interest for numerous applications such as under-water communications, home networks, and space communications [1]–[8]. The pulse position modulation (PPM) [9] system, the on-off keying (OOK) system and the code shift keying (CSK) [10]–[17] system have been investigated as the modulation schemes for OWC with IM/DD technology. PPM conveys information by positioning a pulse in one out of the M time slots. In OOK, the binary symbol is transmitted as the presence or absence of a pulse. CSK using binary signal patterns formed by the rows of binary Hadamard matrices transmits a message by selecting one of M orthogonal signal patterns. It is known that PPM and CSK are superior to OOK because PPM and CSK do not use the threshold detector.

CSK, which is one of the multilevel modulation methods, combines the M-ary orthogonal modulation scheme with spread-spectrum communication technology. CSK uses several pseudo-noise (PN) codes. The data transmission rate of CSK can achieve $\log_2 M$[bit/T_{seq}], where T_{seq} is the duration of PN-code length. Therefore, the data transmission rate and the bit error rate (BER) performance of CSK can improve by increasing the number of PN codes, M. The BER performance of CSK is also better than that of OOK. The BER performance of CSK is much the same as that of PPM in single-user case. Moreover, the multiple access capability of CSK is higher than that of PPM because PPM is prone to interference in multi-access systems.

Considerable research has been carried out on design of the PN code for optical communications such as the optical orthogonal code (OOC) [1], the extended prime code sequence (EPCS) [2]–[4] and the generalized modified prime sequence code (GMPSC) [5], [6]. However, these PN codes are not suitable for optical CSK with IM/DD because the ratio of the number of PN codes (M) and the code length of PN code (L), M/L, is smaller than $1/\sqrt{L}$. Thus, it is difficult to improve the data transmission rate and the error rate of CSK using these PN code. Therefore, one of serious problems encountered with optical wireless CSK with IM/DD is to attain high data transmission rates and good error rates without having to extend the code length.

In order to solve this problem, we propose CSK with a new PN code, which combines GMPSC and Hadamard code. In [18], we analyzed the BER performance of CSK with the new PN code under the additive white Gaussian noise (AWGN) channel. In this paper, we analyze CSK with a new PN code in optical wireless channel. The new PN code can achieve $M/L = 1$. Therefore, it is expected that an optical CSK using the new PN code can achieve high data transmission rate and good error rate compared with the conventional optical CSK systems. In our theoretical analysis, we take scintillation, background-noise, avalanche photo-diode (APD) noise, thermal noise, and signal dependent noise into account. Moreover,we compare the optical CSK system using the new PN code with the conventional optical CSK system.

The outline of this paper is as follows. In Sect. 2, we describe the structure of the new PN code. In Sect. 3, we explain the structure of the optical CSK system with the new PN code. In Sect. 4, we analyze the BER performance. In Sect. 5, we compare with the conventional optical CSK system. Finally, we summarize the main results in Sect. 5.

Manuscript received February 25, 2014.
Manuscript revised July 14, 2014.

†The authors are with the Graduate School of Science and Engineering, Ibaraki University, Hitachi-shi, 316-8511 Japan.
††The author is with the Department of Computer and Information Sciences, College of Engineering, Ibaraki University, Hitachi-shi, 316-8511 Japan.
a) E-mail: 13nm717h@hcs.ibaraki.ac.jp
b) E-mail: 13nm726g@hcs.ibaraki.ac.jp
c) E-mail: habuchi@mx.ibaraki.ac.jp

DOI: 10.1587/transfun.E97.A.2572

Table 1 Notation.

M	The number of pulses of GMPSC
N	The number of GMPSC (= M^2)
M_H	The number of pulses of Hadamard code (= M)
N_H	The number of Hadamard codes (= M)

2. Coding Scheme

In this section, we describe the generation method of the new PN code. Firstly, we explain the structure of GMPSC. Secondly, we explain the structure of the Hadamard code and the extended bi-orthogonal codes. Lastly, we demonstrate the new PN code generation method. Table 1 shows the notation for the following discussion.

2.1 GMPSC

GMPSC [5], [6] is a {0,1}-valued code sequence. GMPSC is divided into M groups, $G_m(m = 1, 2 \cdots M)$. The code length of GMPSC is M^2. Each group has M code sequences. The m-th group, G_m, consists of $g_{m,i}(i = 1, 2 \cdots M)$:

$$G_m = \begin{bmatrix} g_{m,1} \\ g_{m,2} \\ \vdots \\ g_{m,i} \\ \vdots \\ g_{m,M} \end{bmatrix} = \begin{bmatrix} g_{m,11} & g_{m,12} & \cdots & g_{m,1L} \\ g_{m,21} & g_{m,22} & \cdots & g_{m,2L} \\ \vdots & \vdots & \ddots & \vdots \\ g_{m,i1} & g_{m,i2} & \cdots & g_{m,iL} \\ \vdots & \vdots & \ddots & \vdots \\ g_{m,M1} & g_{m,M2} & \cdots & g_{m,ML} \end{bmatrix} \tag{1}$$

$g_{m,i}(i = 1, 2 \cdots M)$ is a {0,1}-value code sequence with the code length $L(= M^2)$. The number of positive-value chips becomes M in every code sequence. And further, the cross correlation function, $I_{g_{m,i}g_{n,j}}$, between $g_{m,i}$ and $g_{n,j}$ is

$$I_{g_{m,i}g_{n,j}} = \begin{cases} M & (m = n \cap i = j) \\ 0 & (m = n \cap i \neq j) \\ 1 & (\text{otherwise}). \end{cases} \tag{2}$$

2.2 Hadamard Code

An Hadamard code H_M, which is generated by $M \times M$ Hadamard matrix, is a {1, −1}-valued orthogonal code sequence. The Hadamard matrix of order M, H_M, is

$$H_M = \begin{bmatrix} H_{\frac{M}{2}} & H_{\frac{M}{2}} \\ H_{\frac{M}{2}} & \overline{H_{\frac{M}{2}}} \end{bmatrix} = \begin{bmatrix} h_{11} & h_{12} & \cdots & h_{1M} \\ h_{21} & h_{22} & \cdots & h_{2M} \\ \vdots & \vdots & \ddots & \vdots \\ h_{M1} & h_{M2} & \cdots & h_{MM} \end{bmatrix} \tag{3}$$

where $\overline{H}$ is the negative of H.

The initial Hadamard matrix of order $M = 1$, H_1 is 1. Moreover, H_2 is expressed as

$$H_2 = \begin{bmatrix} +1 & +1 \\ +1 & -1 \end{bmatrix}. \tag{4}$$

M binary code sequences derived from rows of Hadamard matrix of order M become the orthogonal signals. And, these M rows plus their complements form a $2M$ bi-orthogonal set. Therefore, the Hadamard matrix of order M, H_M, has M orthogonal signals and also forms a $2M$-ary bi-orthogonal set, B_M. B_M is expressed as

$$B_M = \begin{bmatrix} H_M \\ \overline{H_M} \end{bmatrix} = \begin{bmatrix} h_{11} & h_{12} & \cdots & h_{1M} \\ h_{21} & h_{22} & \cdots & h_{2M} \\ \vdots & \vdots & \ddots & \vdots \\ h_{M1} & h_{M2} & \cdots & h_{MM} \\ \overline{h_{11}} & \overline{h_{12}} & \cdots & \overline{h_{1M}} \\ \overline{h_{21}} & \overline{h_{22}} & \cdots & \overline{h_{2M}} \\ \vdots & \vdots & \ddots & \vdots \\ \overline{h_{M1}} & \overline{h_{M2}} & \cdots & \overline{h_{MM}} \end{bmatrix}. \tag{5}$$

2.3 New PN Code

The new PN code is generated by following four steps.

Firstly, we generate matrix, which diagonal element is vector $g_{m,i}$ in Eq. (1).

$$\begin{bmatrix} g_{m,i1} & 0 & \cdots & 0 \\ 0 & g_{m,i2} & \cdots & 0 \\ \vdots & \vdots & \ddots & \vdots \\ 0 & 0 & \cdots & g_{m,iL} \end{bmatrix} \tag{6}$$

Secondly, in Eq(5), h_{ij} is replaced by

$$h_{ij} \rightarrow \overbrace{h_{ij}, h_{ij}, h_{ij} \cdots h_{ij}}^{M}. \tag{7}$$

We obtain $2M \times M^2$ matrix, denoted a extended bi-orthogonal matrix, C_M, by the above replacement. The extended bi-orthogonal matrix, C_M, has $2M$ bi-orthogonal code $c_j(j = 1, 2, \cdots, 2M)$ and is expressed as

$$C_M = \begin{bmatrix} c_1 \\ c_2 \\ \vdots \\ c_j \\ \vdots \\ c_M \\ c_{M+1} \\ c_{M+2} \\ \vdots \\ c_{M+j} \\ \vdots \\ c_{2M} \end{bmatrix} = \begin{bmatrix} \overbrace{h_{11} \cdots h_{11}}^{M} \cdots \overbrace{h_{1M} \cdots h_{1M}}^{M} \\ h_{21} \cdots h_{21} \cdots h_{2M} \cdots h_{2M} \\ \vdots \\ h_{j1} \cdots h_{j1} \cdots h_{jM} \cdots h_{jM} \\ \vdots \\ h_{M1} \cdots h_{M1} \cdots h_{MM} \cdots h_{MM} \\ \overline{h_{11}} \cdots \overline{h_{11}} \cdots \overline{h_{1M}} \cdots \overline{h_{1M}} \\ \overline{h_{21}} \cdots \overline{h_{21}} \cdots \overline{h_{2M}} \cdots \overline{h_{2M}} \\ \vdots \\ \overline{h_{j1}} \cdots \overline{h_{j1}} \cdots \overline{h_{jM}} \cdots \overline{h_{jM}} \\ \vdots \\ \overline{h_{M1}} \cdots \overline{h_{M1}} \cdots \overline{h_{MM}} \cdots \overline{h_{MM}} \end{bmatrix}. \tag{8}$$

Thirdly, the new PN code, denoted $GH_m(i, j)$, is generated by multiplying Eq. (6) by vector c_j in Eq. (8). $GH_m(i, j)$ is expressed as

$$GH_m(i, j) = \begin{bmatrix} g_{m,i1} & 0 & \cdots & 0 \\ 0 & g_{m,i2} & \cdots & 0 \\ \vdots & \vdots & \ddots & \vdots \\ 0 & 0 & \cdots & g_{m,iL} \end{bmatrix} c_j^{\mathrm{T}}$$
$$= \left[\, g_{m,i1}h_{j1} \;\; g_{m,i2}h_{j1} \;\; \cdots \;\; g_{m,iL}h_{jM} \,\right]^{\mathrm{T}} \tag{9}$$

As a result, $GH_m(i, j)$ becomes $\{-1, 0, 1\}$-valued code sequence.

Lastly, in order to apply $GH_m(i, j)$ in optical wireless channel, $GH_m(i, j)$ is converted into non-negative signal. The elements 0 are replaced with 00 in the code sequence, 1 with 10 and -1 with 01. The code generated becomes the new PN code, $OGH_m(i, j)$.

Since the new PN code $OGH_m(i, j)(i = 1, 2, \cdots, M$ and $j = 1, 2, \cdots, 2M)$ is the $\{0,1\}$-valued code sequence, it can be adopted as PN code in the optical wireless communication. Furthermore, since each group consists of $2L(= 2M^2)$ code sequences with code length $2L$, CSK using the new PN code $OGH_m(i, j)$ can achieve high data transmission rate and good error rate in comparison to the optical CSK using conventional PN code. Moreover, $OGH_m(i, j)(i = 1, 2, \cdots, M$ and $j = 1, 2, \cdots, 2M)$ constitute a set of $2M^2$ biorthogonal signals.

For example, we show the new PN code structured by combing GMPSC with code length $L = 16$ with Hadamard code of order 4. GMPSC is divided into 4 groups, $G_m(m = 1, 2, 3, 4)$. The first group G_2 is

$$G_2 = \begin{bmatrix} g_{2,1} \\ g_{2,2} \\ g_{2,3} \\ g_{2,4} \end{bmatrix} = \begin{bmatrix} 1000010000100001 \\ 0100100000010010 \\ 0010000110000100 \\ 0001001001001000 \end{bmatrix}. \tag{10}$$

The bi-orthogonal sequence, B_4, is obtained by the Hadamard code H_4:

$$B_4 = \begin{bmatrix} 1 & 1 & 1 & 1 \\ 1 & -1 & 1 & -1 \\ 1 & 1 & -1 & -1 \\ 1 & -1 & -1 & 1 \\ -1 & -1 & -1 & -1 \\ -1 & 1 & -1 & 1 \\ -1 & -1 & 1 & 1 \\ -1 & 1 & 1 & -1 \end{bmatrix} \tag{11}$$

Therefore, the extended bi-orthogonal code, C_4, is expressed as

$$C_4 = \begin{bmatrix} c_1 \\ c_2 \\ c_3 \\ c_4 \\ c_5 \\ c_6 \\ c_7 \\ c_8 \end{bmatrix} = \begin{bmatrix} 1&1&1&1&1&1&1&1&1&1&1&1&1&1&1&1 \\ 1&1&1&1&-1&-1&-1&-1&1&1&1&1&-1&-1&-1&-1 \\ 1&1&1&1&1&1&1&1&-1&-1&-1&-1&-1&-1&-1&-1 \\ 1&1&1&1&-1&-1&-1&-1&-1&-1&-1&-1&1&1&1&1 \\ -1&-1&-1&-1&-1&-1&-1&-1&-1&-1&-1&-1&-1&-1&-1&-1 \\ -1&-1&-1&-1&1&1&1&1&-1&-1&-1&-1&1&1&1&1 \\ -1&-1&-1&-1&-1&-1&-1&-1&1&1&1&1&1&1&1&1 \\ -1&-1&-1&-1&1&1&1&1&1&1&1&1&-1&-1&-1&-1 \end{bmatrix}. \tag{12}$$

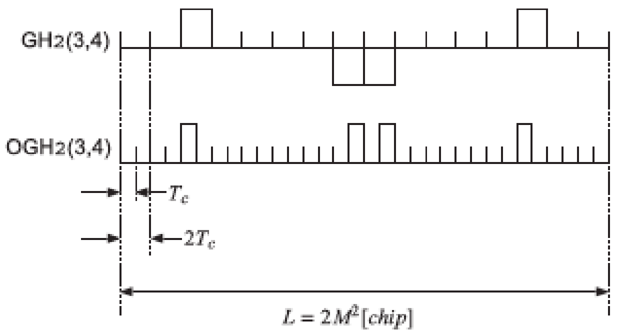

Fig. 1 Example of the new PN codes ($GH_2(3, 4)$, $OGH_2(3, 4)$).

$GH_2(3, 4)$ obtained by $g_{2,3}$ in Eq. (10) and c_4 in Eq. (12) is expressed as

$$GH_2(3, 4) = [0\,0\,1\,0\,0\,0\,0\,-1\,-1\,0\,0\,0\,0\,1\,0\,0]^{\mathrm{T}}.$$

Thus, the new PN code with non-negative signal, $OGH_2(2, 4)$, is obtained from $GH_2(3, 4)$,

$$OGH_2(3, 4) = [00001000000000010100000000100000]^{\mathrm{T}}.$$

Figure 1 illustrates $GH_2(3, 4)$ and $OGH_2(3, 4)$.

3. System Structure

Figure 2 illustrates the system model of the proposed system.

In the transmitter, firstly, source data are divided into DATA1($\log_2 M$[bit]) and DATA2($\log_2 2M$[bit]). Secondly, in m-th group of GMPSC, one of the M code sequences is selected according to DATA1. One of the $2M$ extended bi-orthogonal code sequences is selected by DATA2. Thirdly, $GH_m(i, j)$ is generated by the selected GMPSC and the selected extended bi-orthogonal code. Fourthly, $GH_m(i, j)$ is multiplied by the manchester coded signal in each 1 chip. Lastly, after the multiplied signals pass through circuit that forms a non-negative signal, $OGH_m(i, j)$ is generated. This code is transmitted to the receiver through an optical wireless channel.

In the receiver, it contains M correlators for GMPSC, each one corresponds to one of the possible M GMPSC. Moreover, the receiver also has other M correlators for the extended bi-orthogonal codes. The correlation value are converted into the electrical signal at every chip duration by APD for chip level detection [17]. The converted signal is multiplied by reference signal in each 2 chips. In the GMPSC detector, these magnitudes of M correlator outputs are examined and the largest one is selected. Therefore, DATA1 is demodulated by correlating the received signal with GMPSC. In the extended bi-orthogonal code detector, $g_{m,i}$ is determined by using the estimated GMPSC. DATA2 is demodulated by correlating the received signal with M-extended bi-orthogonal codes of $g_{m,i}$.

4. Performance Analysis

In this section, we analyze the bit error rate (BER) performance in an optical channel.

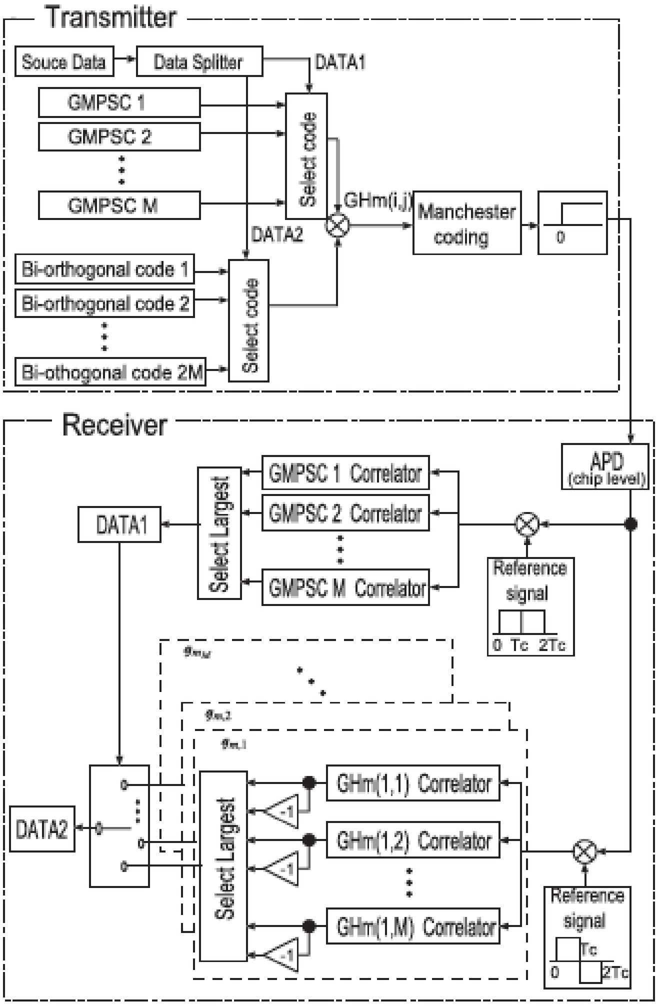

Fig. 2 System structure of CSK with the new PN code.

4.1 Channel Model

In our theoretical analysis, we take into account scintillation, background-noise, avalanche photo-diode (APD) noise, thermal noise, and signal dependent noise. The probability that a specified number of photons are absorbed from an incident optical field by an APD detector over a chip interval with T_c is given by a Poisson distribution [8]. We assume that the APD output during each chip interval is Gaussian random variable, so, the correlator output, which is the accumulated output during each chip interval, is also a Gaussian random variable.

In the optical wireless communication, we need to take into account the scintillation which influences the attenuation and the fluctuation of the received optical power. The scintillation X characterized by the stationary probability process. Its probability density function $p(X)$ can be written as [9]

$$p(X) = \frac{1}{\sqrt{2\pi\sigma_s^2 X}}\exp\left\{-\frac{(\ln X + \sigma_s^2/2)^2}{2\sigma_s^2}\right\} \tag{13}$$

where the average of scintillation X is normalized to unity, and σ_s^2 is logarithm variance. The variance σ_s^2 is determined by the atmospheric state.

The average $\mu[P_{in}]$ of the electrons emitted by APD is given by the following equation.

$$\mu[P_{in}] = GT_c\left(\frac{\eta P_{in}}{hf} + \frac{I_b}{e}\right) + \frac{I_s T_c}{e} \tag{14}$$

where, P_{in} is the received laser power, G is the average APD gain, hf is the energy of a single photon, η is the quantum yield, e is the electronic charge, I_b is the average bulk leakage current and I_s is the average surface leakage current.

The variance $\sigma^2[P_{in}]$ of the electrons emitted by APD is given by the following equation.

$$\sigma^2[P_{in}] = G^2 FT_c\left(\frac{\eta P_{in}}{hf} + \frac{I_b}{e}\right) + \frac{I_s T_c}{e} + \frac{2k_B T_r T_c}{e^2 R_L} \tag{15}$$

Where, k_B is the Boltzmann constant, T_r is the receiver's noise temperature and R_L is the load resistance. In above equation, F is the excess noise index, which can be expressed as below

$$F = k_{eff}G + (1 - k_{eff})\left(\frac{2G-1}{G}\right) \tag{16}$$

where, k_{eff} is the effective ionization coefficient. The third term of Eq. (14) represents thermal noise.

When P_w is the received optical power without the effect of scintillation and background noise and P_b is the background noise, P_{in} can be expressed as follows

$$P_{in} = \begin{cases} P_w X + P_b & for\ a\ mark \\ \frac{P_w X}{M_e} + P_b & for\ a\ space \end{cases} \tag{17}$$

where M_e is the modulation loss rate.

4.2 Bit Error Rate

In the proposed system, BER is obtained by the estimation error of GMPSC for DATA1 and the estimation error of the extended bi-orthogonal code for DATA2.

The estimation error rate of DATA1, denoted SER_1, can be written as

$$SER_1 = \int_0^{\infty} p(X) \int_{-\infty}^{\infty} \frac{1}{\sqrt{\pi}}\exp\left(-z^2\right) \left\{\frac{1}{2}\mathrm{erfc}\left(-\frac{\sqrt{\sigma_1{}^2(X)}}{\sqrt{\sigma_m{}^2(X)}}z - \frac{\mu_1(X) - \mu_m(X)}{\sqrt{2\sigma_m{}^2(X)}}\right)\right\}^{M-1} dz\,dX \tag{18}$$

In Eq. (17), the average and the variance of correlator output $\mu_1(X), \sigma_1{}^2(X), \mu_m(X), \sigma_m{}^2(X)$ can be written as below from Eqs. (13) and (14).

$$\mu_1(X) = M\mu\left[P_w X + P_b\right] + M\mu\left[\frac{P_w X}{M_e} + P_b\right]$$

$$\sigma_1{}^2(X) = M\sigma^2[P_\omega X + P_b] + M\sigma^2\left[\frac{P_\omega X}{M_e} + P_b\right]$$
$$\mu_m(X) = 2M\mu\left[\frac{P_\omega X}{M_e} + P_b\right]$$
$$\sigma_m{}^2(X) = 2M\sigma^2\left[\frac{P_\omega X}{M_e} + P_b\right]$$

Therefore, the bit error rate of DATA1, denoted BER_1, is given by

$$BER_1 = \frac{1}{2}SER_1.$$

The estimation error of DATA2, SER_2 depends on SER_1.

When DATA1 is correct, the estimation error rate of DATA2, denoted SER_2, can be written as

$$SER_2 = 1 - \int_0^\infty p(X)\int_{-\frac{\mu_1(X)}{\sqrt{\sigma_1{}^2(X)}}}^\infty \frac{1}{\sqrt{\pi}}\exp\left(-z^2\right) \left\{1 - \mathrm{erfc}\left(z + \frac{\mu_1(X)}{\sqrt{2\sigma_m{}^2(X)}}\right)\right\}^{M-1} dzdX \tag{19}$$

In Eq. (18), the average and the variance of correlator output $\mu_1(X), \sigma_1{}^2(X), \sigma_m{}^2(X)$ can be written as below from Eqs. (13) and (14).

$$\mu_1(X) = M\mu[P_\omega X + P_b] - M\mu\left[\frac{P_\omega X}{M_e} + P_b\right]$$
$$\sigma_1{}^2(X) = M\sigma^2[P_\omega X + P_b] + M\sigma^2\left[\frac{P_\omega X}{M_e} + P_b\right]$$
$$\sigma_m{}^2(X) = \sigma_1{}^2(X)$$

Therefore, the bit error rate of DATA2, denoted BER_2, is given by

$$BER_2 = \frac{1}{2}SER_2(1 - SER_1) + \frac{1}{2}SER_1.$$

Therefore, the average BER of CSK using new PN code is expressed as

$$BER = \frac{\log_2 M}{\log_2 M + \log_2(2M)}BER_1 + \frac{\log_2(2M)}{\log_2 M + \log_2(2M)}BER_2. \tag{20}$$

5. Numerical Results

In this section, we show the results from theoretical analysis of the bit error rate (BER) performance. The numerical results of the proposed system are obtained by calculating Eq. (20). Table 2 shows the numerical parameters for evaluation. We use typical APD parameters [7], [9]. We assume that the chip duration is $1/(156\times L)$ [μsec], where L is length of PN code.

Figure 3 shows BER versus average received laser power per bit. We make a comparison of the propoaed system (L =32, 128, 512) and CSK using GMPSC (L =16, 64, 256). Since the number of codes of the proposed system is greater than that of CSK using GMPSC at the same code length, BER of the proposed system is better than that of CSK using GMPSC. Moreover, the data transmission rate, R_p, of the proposed system is higher than the data transmission rate, R_g, of CSK using GMPSC; $R_p = (\log_2 M + \log_2 2M)/(LT_c)$ [bit/sec] and $R_g = \log_2 M/(LT_c)$ [bit/sec]. Although BER of the proposed system (L = 32) is the same as that of CSK using GMPSC (L = 256), the data transmission rate of the proposed system (L = 32) is higher than that of CSK using GMPSC (L = 256); $R_p = 5 \times 156$ [Mbps] and $R_g = 4 \times 156$ [Mbps]. Therefore, the proposed system is superior to CSK using GMPSC.

Figure 4 shows BER versus average received laser power per bit. We make a comparison of the proposed system (L = 32, 128, 512) and CSK using Hadamard code (L = 32, 128, 512). As a result, BER of the proposed system is better than that of CSK using Hadamard code, because the variance $\sigma_1^2(X)$ of the

Table 2 Notation.

Name	Symbol	Value
Laser wavelength		830 [nm]
Background noise	P_b	−45 [dBm]
Quantum efficiency	eta	0.6
Scintillation logarithm variance	σ_s^2	0.01
APD Gain	G	100
Effective ionization ratio	k_{eff}	0.02
Bulk leakage current	I_b	0.1 [nA]
Surface leakage current	I_s	10 [nA]
Modulation extinction ratio	Me	100
Receiver noise temperature	T_r	1100 [K]
Receiver load resistor	RL	1030 [Ω]

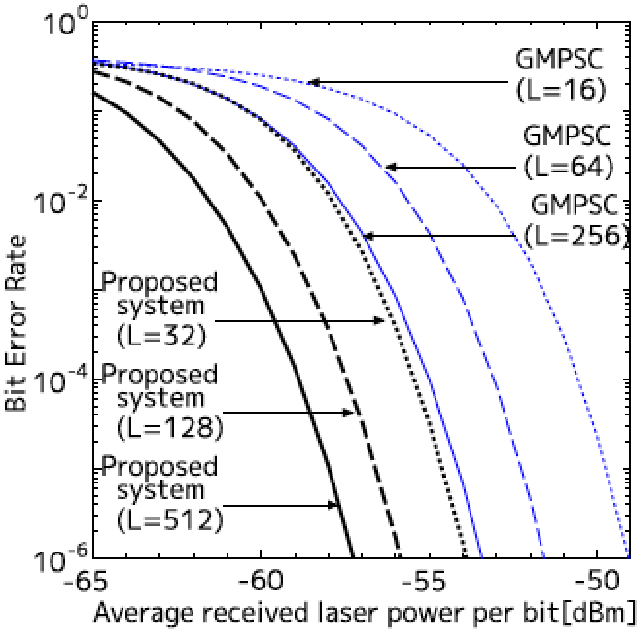

Fig. 3 BER versus average received laser power per bit, where L = 16, 32, 64, 128, 256 and 512.

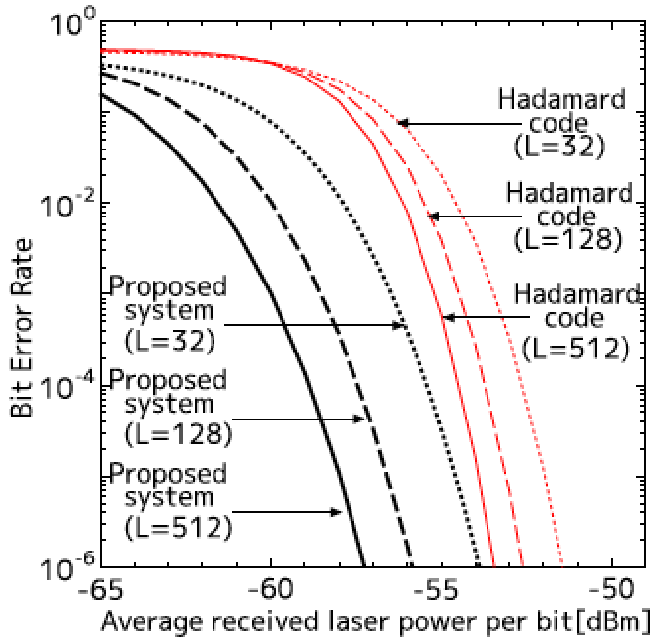

Fig.4 BER versus average received laser power per bit, where L = 32, 128 and 512.

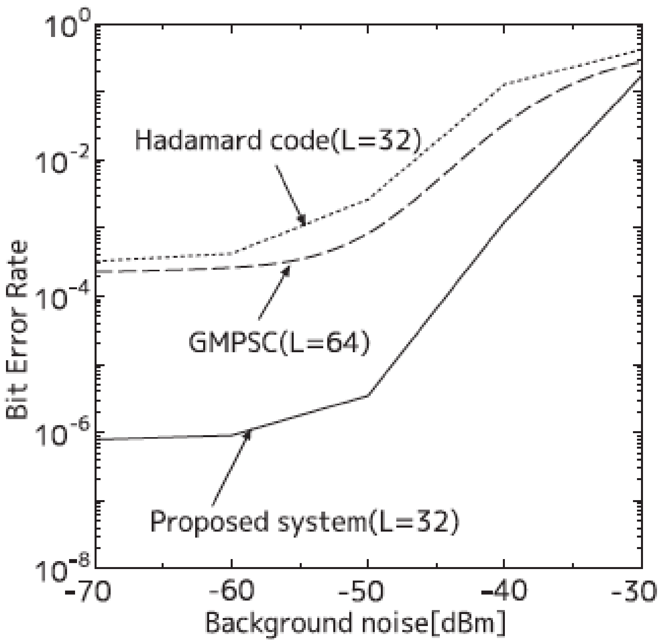

Fig.5 BER versus Background noise (P_b) when average received laser power per bit (P_{bit}) = −55 [dBm], and L = 32 and 64.

proposed system is smaller than the variance σ_a^2 of CSK using Hadamard code; $\sigma_a^2 = .M^2\sigma^2[(1/M)P_\omega X + P_b] + M^2\sigma^2[(1/M)P_\omega X/M_e + P_b]$. Moreover, the data transmission rate, R_p, of the proposed system is equal to the data transmission rate, R_h, of CSK using Hadamard code. Therefore, the proposed system outperforms CSK using Hadamard code.

Figure 5 shows BER when average received laser power per bit is −55 [dBm]. We make a comparison of the proposed system (L = 32) and CSK using GMPSC (L = 16) and CSK using Hadamard code (L = 32). As a result, BER versus Background noise (P_b) of the proposed system is better than that of CSK using GMPSC and that of CSK using Hadamard code.

6. Conclusion

In this paper, we have proposed the optical CSK using a new PN code, which combines GMPSC with Hadamard code. The new PN code can achieve M/L = 1. we analyze the BER performance of the proposed system. In our theoretical analysis, we take into account scintillation, background-noise, avalanche photo-diode (APD) noise, thermal noise, and signal dependent noise. It is found that the proposed system outperforms the conventional optical CSK using the Hadamard codes with uni-polar signalling and the conventional optical CSK using GMPSC. In future works, we will analyze N parallel code shift keying using new PN code in order to improve data transmission rate. Moreover, we investigate the combination of turbo codes and the new PN code.

Acknowledgment

This study was supported in part by Grant-in-Aid for Scientific Research (C).

References

[1] J.A. Slalehi, "Code division multiple-access techniques in optical fiber networks," IEEE Trans. Commun., vol.37, no.8, pp.824–833, Aug. 1989.
[2] W.C. Kwong, P.A. Perrier, and P.R. Prucnal, "Performance comparison of asynchronous and synchronous code-division multiple-access techniques for fiber-optic areanetworks," IEEE Trans. Commun., vol.39, no.11, pp.1625–1634, Nov. 1991.
[3] G.-C. Yang and W.C. Kwong, "Performance analysis of optical CDMA with prime codes," Electron. Lett., vol.31, pp.569–570, 1995.
[4] A.A. Shaar, "Prime sequences: Quasi-optical sequences for OR channel code division multiplexing," IEEE Electron. Lett., vol.19, pp.888–889, Oct. 1983.
[5] T. Matsushima, T. Nagao, N. Ochiai, and Y. Teramachi, "Generalization of modified prime sequence codes and its properties," IEICE Trans. Fundamentals (Japanese Edition), vol.J91-A, no.5, pp.559–573, May 2008.
[6] T. Matsushima and Y. Teramachi, "Codes with unique correlation property and their application," IEICE Technical Report, WBS2009-77, March 2010.
[7] H.M.H. Shalaby, "Chip-level detection in optical code division multiple access," J. Lightwave Technol., vol.16, no.6, pp.1077–1087, June 1998.
[8] H.M. Kwon, "Optical orthogonal code-division multiple-access system part1: APD noise and thermal noise," IEEE Trans. Commun., vol.42, no.7, pp.2470–2479, July 1994.
[9] T. Ohtsuki, "Performance analysis of atmospheric optical PPM CDMA systems," J. Lightwave Technol., vol.21, no.2, pp.406–411, Feb. 2003.
[10] H. Habuchi and F. Ono, "Optical code shift keying with modified prime sequences," IEICE Technical Report, WBS2003-74, Oct. 2003. (in Japanese)
[11] Y. Kozawa and H. Habuchi, "Theoretical analysis of M-CSK/CDMA

system in optical wireless channel," International Symposium on Information Theory and its Applications (ISITA 2010), pp.738–742, Oct. 2010.
[12] N. Ochiai, S. Kushibiki, T. Matsushima, and Y. Teramachi, "Performance analysis of synchronous optical CDMA system withe EWO signaling," IEICE Trans. Fundamentals (Japanese Edition), vol.J86-A, no.9, pp.957–968, Sept. 2003.
[13] T. Yamashita, M. Hanawa, Y. Tanaka, and M. Takahara, "An optical code division multiplexing system using Hadamard codes and SIK," IEICE Technical Report, OCS98-1, May 1998. (in Japanese)
[14] R. Menendez, A. Agarwal, P. Toliver, J. Jackel, and S. Etemad, "Direct optical processing of M-ary code-shift-keyed spectral-phase-encoded OCDMA," J. Optical Networking, vol.6, no.5, pp.442–450, May 2007.
[15] B. Dai, Z. Gao, X. Wang, and N. Wada, "Demonstration of differential detection on attacking code-shift-keying OCDMA system," Electron. Lett., vol.46, pp.1680–1682, Dec. 2010.
[16] Y. Kozawa and H. Habuchi, "A study on optical atmospheric synchronous CSK/SSMA with extended prime code sequences," 31st Symposiumon Information Theory and its Applications (SITA2008), no.2.3.1, pp.159–163, Oct. 2008.
[17] Y. Kozawa and H. Habuchi, "Enhancement of optical wireless N-CSK system," 8th IEEE Asia Pacific Wireless Communications Symposium (APWCS 2011), Aug. 2011.
[18] Y. Takamaru and H. Habuchi, "Design of PN codes for optical wireless code-shift-keying with IM/DD," Proc. International Workshop on Signal Design and its Application (IWSDA 2013), Oct. 2013.

Yusuke Takamaru was born in Ibaraki, Japan on September 29, 1990. He received B.E. degree from Ibaraki University in 2013. He is currently working toward an M.E. degree at Ibaraki University. His research interests are in Optical wireless Communications and Spread-Spectrum Communications.

Sachin Rai earned his Bachelor's degree in Information Management (BIM) from Tribhuvan University, Kathmandu, Nepal in December 2007. He is currently enrolled as a Master's student in Graduate School of Science and Engineering, Ibaraki University, Japan. His major is Computer Science and Information Engineering. His research interests include Optical Wireless Communication (OWC), Error Correction Codes, and IP Communications.

Hiromasa Habuchi was born in Hyogo, Japan, on July 4, 1963. He received the B.E., M.E. and Ph.D. degrees in Electrical Engineering from Saitama University, in 1987, 1989 and 1992, respectively. He joined in Faculty of Engineering, Ibaraki University in 1992 as a research associate. He was an associate professor at the same university in 1998–2010. He is currently a professor of computer science. Dr. Habuchi received the IEICE Young Engineer Award in 1995 and the YRP Award in 2007. He is a member of IEICE, IEEE and SITA (The Society of Information Theory and its Applications, Japan). His research interests are in Spread-Spectrum Communications, Ambient Communications, Synchronization Systems, M-ary Communications and Optical Communications.

Ⅱ.プロジェクト業績

1. 活動内容

【都市インフラの強靭化技術開発】
炭素繊維やパサルト繊維による構造補強材の高性能化により、インフラ構造物の耐震性やResilience（自己回復性）向上手法を開発し、都市インフラの強靭化技術に関する取り組みを行っており、産学連携を検討している。（呉教授）

【都市インフラモニタリングや知能化による高度化センサ技術の開発】
1）光ファイバセンサ方式とカーボンファイバセンサ方式による長寿命・高性能化された分布型領域センサの実製作・性能究明および実用性を実験室レベルで検討した。
２）領域センサにより得られるひずみ分布の直接利用により、構造物の早期損傷検知に対する各種指標を検討した。
３）開発したセンサ、装置、検知アルゴリズムを基に、早期損傷検知システムを開発し、茨城県内の RC 桁橋、新潟県内の既損傷 PC 箱桁橋、東北新幹線高架橋、中国の蘇通大橋（１０００ｍ級長大橋）など既設構造物のリアルタイム健全性評価システムの検証を進めている。
４）高度化された光ファイバ分布センシング技術による広域地圏環境（河川堤防・地すべり）防災システムの構築に関する産官学連携プロジェクトを開始し、基礎検討を行っている。
（呉教授）

【センサデータの安定した通信/解析技術の開発と省電力化推進】

1) 大規模災害により、電源インフラが完全消失した状況において、市民にどのように、情報を伝達するか、また市民の安否情報をどのように収集するかについて研究を進めている。内部電源を必要としない UHF 帯 RFID を利用している。（武田教授）

【老朽化したインフラ構造物の災害リスクを考慮した維持管理計画】

1) 橋梁の（異常監視）ヘルスモニタリングシステムの実証実験を常陸大宮市の引田橋での継続的に実施した。（齋藤特命教授,原田准教授, 鎌田教授）
2) ひたちなか海浜鉄道湊線での企業との傾斜計の実証実験を推進. 本件は 10 月に茨城県土木部との連携で常陸大宮地区の地すべり危険地域への応用予定（齋藤特命教授）
3) 構造物の耐久性設計に資する高度化シミュレーション技術を開発している（車谷准教授）

【UAV を活用した新たな空間情報の防災システムへの活用と超小型衛星との連携】

1) 茨城県生活安全部と UAV による安全監視・不法投棄防止システムの実現の連携検討を開始した。（齋藤特命教授）
2) 宮城教育大学との UAV を用いた空間環境情報可視化と津波災害地域の空撮を行った。（齋藤特命教授）
3) 宮城県石巻市、女川町での空撮による災害地域の土地利用変化、震災遺構の映像保存プロジェクトをスタートさせた。（齋藤特命教授）

【アウトリーチとしての防災・減災、それらを含む環境教育の実施】

1) 日本リモートセンシング学会との共催で、守谷市内小学校で防災における空間情報応用に関する講演を実施した。（桑原准教授）
2) ひたちなか市外野小学校、前渡小学校にて環境・情報教育を実施した。（齋藤特命教授、桑原准教授）
3) (社)次世代センサ協議会第 44 回センサ＆アクチュエータ技術シンポジウムにて UAV と防災について講演した。（齋藤特命教授）
4) 日本リモートセンシング学会との共催で、守谷市内小学校で防災における空間情報応用に関する講演を実施した。（桑原祐史准教授）

【災害時および平常時等における情報共有法】
1) 防災情報を配信する方法には、インターネットやＦＭ放送、拡声器などを利用する方法があるが一長一短がある。そこで追加手段の１つとして交通信号機を配信局として用いる方法を研究している。特に、光点滅（ＬＥＤのオンオフ、人間の目ではそのオンオフは感知できない）による光ワイヤレス通信の高信頼化について検討している。
2) 大規模震災では、集中制御が基となる携帯網・ワイヤレス通信網では情報共有は難しいまた、信号機等の停電により大規模な車両渋滞が生じると考えられる。その渋滞車両を積極的に通信局として利用するネットワーク網を構築する研究を進めている。ＭＡＣプロトコルとして、変形２進カウントダウン法を考案している。（羽渕裕真教授）

【地元企業・学校等との学術連携実現】

1) 日立製作所と連携し、ベトナム国ダナンおよびビンディン県の防災システム構築に参加した。（桑原准教授）
2) 湊線の鉄道運行支援システム構築について、連携研究を実現（ひたちなか海浜鉄道、福山 C）した。（齋藤特命教授，桑原准教授）

【他大学・企業・自治体連携での研究資金獲得】

1) 東北大学と共同で申請した科研費（挑戦的萌芽）「地盤中の間隙水の挙動調査」採択（東北大学風間基樹教授，茨城大学安原一哉名誉教授，鎌田賢教授）（齋藤修特命教授の企画・アレンジによる）において、地中埋め込み型の土砂内水流・水圧センサと無線モジュールを開発した。
2) 日本リモートセンシング学会の後援として、仙台市（東北工業大学）にて防災に対する衛星画像利用の WS を開催した。（桑原准教授）
3) シンポジウム「SICE 計測部門セミナー 都市のスマートセンシング」を企画して開催した。（齋藤特命教授）
   http://rcl.it.aoyama.ac.jp/sice-sss/sice_seminar_20140917.html

【自治体との各種連絡会議推進（茨城県・日立市・ひたちなか市等）】

1) 茨城県商工労働部、土木部、企画部、生活安全部との定期情報交換（齋藤特命教授）（鎌田教授，桑原准教授は随時参加）
2) 日立市土木部、生活環境部、市長、副市長との定期情報交換（齋藤特命教授）（鎌田教授，桑原准教授は随時参加）
3) ひたちなか市長との情報交換会 1 回／年度（齋藤特命教授）（鎌田教授，桑原准教授は随時参加）

【国際共同研究を実施（アメリカ、英国、イタリア、中国、韓国等）】

1) 科研 S-8(安原名誉教授)におけるメコン川流域とメコンデルタの気候変動影響と災害事情調査(UAV による調査を含む)に参画した。成果は 2014 年 8 月 30 日 NHK-TV　NHK スペシャルにて放映された。
2) センシング技術による地下鉄防災システムの高度化に関する共同研究を英国のケンブリッジ大学、長大橋の長寿命化に関する研究を中国の東南大学、光ファイバ技術による高速道路橋の長期モニタリングに関してアメリカＦＨＷＡ（連邦道路管理局）橋梁の長期性能検討プロジェクトチームなどと共同研究を推し進めている。（呉教授他）

【大学院生の教育】

1）５名の社会人博士課程入学者をリクルートした 2013 年度につづき、2014 年度には 3 名の社会人博士課程入学者をリクルートした。（齋藤特命教授）センター教員の連携による指導体制を構築している。

2）当センター所属院生を中心にして、茨城大学学生国際会議（１１月１５日１６日：水戸キャンパス）の企画・運営を行った。（呉教授、沼尾教授、鎌田教授、湊教授、桑原准教授、外岡准教授）

3）羽渕研究室学部 4 年生 高柳翔太君の研究成果発表「ＬＥＤのオンオフ信号による光ワイヤレス通信の研究成果」が電子情報通信学会東京支部学生会学生奨励賞を受賞した。（全発表数数：２２９、受賞者数：２１）

4）羽渕研究室博士前期課程 2 年生 ライ サチン君の国際会議発表「Proposal of Turbo-Coded Differential OOK for Optical IM/DD System」が RISP International Workshop on Nonlinear Circuits, Communications and Signal Processing (NCSP'15)にて Student Paper Award を受賞した。

2. 実績一覧

【学術誌論文】

1） 野口宏，大瀧保広，鎌田賢: BCP としての学内データセンターの設置とその活用方針，学術情報処理研究, 18, 24－32 (Sep. 2014).

2） 須藤翔太，小玉駿，福田貴大，渋沢進，鎌田賢，米倉達広，歩行者の位置に応じて情報を正対表示するシステム，電子情報通信学会論文誌(A)，Vol.J98-A，No.1，pp.129-134，Jan. 2015.

3） コンクリートのひび割れ進展計測のための画像解析手法に関する基礎的研究，車谷麻緒，松浦遵，根本忍，呉智深，土木学会論文集 A2(応用力 学)，印刷中.

4） 異形鉄筋周辺のコンクリートに形成する内部ひび割れモードの再現シミュレーション，車谷麻緒，根本優輝，岡崎慎一郎，日本計算工学会論文 集，Vol.2014,pp.20140008, 2014.

5） 微細ひび割れの形成と接触を考慮した準脆性材料の圧縮破壊シミュレーション，神野真弥，車谷麻緒，寺田賢二郎，京谷孝史，樫山和男，日本計算 工学会論文集，Vol.2014, pp.20140006, 2014.

6） Kyohei Sumikawa and Hiromasa Habuchi： Influence of Scintillation and Background Noise on LDGM-BPPM with Unequal Transmission Power Allocation Scheme in Optical Wireless Channel, Journal of Signal Processing, Vol.18, No.4, pp.181-184 (2014)

7） Yusuke Takamaru, Sachin Rai and Hiromasa Habuchi :Theoretical Analysis of New PN Code on Optical Wireless Code-Shift-Keying, IEICE Transaction on Fundamentals, Vol.E97-A, No.12, pp.2572-2578, (2014-12)

8） Kyohei Sumikawa and Hiromasa Habuchi： Optical Wireless LDGM-BPPM With Unequal Transmission Power Allocation Scheme, IEICE Transaction on Fundamentals, Vol.E97-A, No.12, pp.2579-2585, (2014-12)

9） An Arafa M. A. Ibrahim, Zhishen Wu, Mohamed F. M. Fahmy, and Doaa Kamal: Experimental Study on the Structural Performance of Concrete Bridge Columns Reinforced by Hybrid Steel and FRP Reinforcements. Composites for Construction, ASCE Journal. (submitted)

10） Arafa M. A. Ibrahim, Mohamed F. M. Fahmy and Zhishen Wu: Bond-Based Study on Hybrid FRP and Steel Bars as Main Reinforcement for Bridge Columns. Journal of Composite Structures. (submitted)

11） Huang Huang, Zhishen Wu and Ryota Tagayanegi: Fiber model-based identifications for flexural behavior of reinforced concrete columns with self-sensing basalt-fiber-reinforced polymer bars. Smart Materials and Structures. (submitted)

12） H. Huang, Z.S. Wu and K. Kishida: Wavelet-based signal processing of high-sampling-rate strain measurements of BOTDA-based distributed fiber-optic sensing. Optical Fiber Technology. (submitted)

【招待講演】

1） Zhishen Wu: Advancement of Fibre Optic sensing technology for health monitoring of civil structures. The Cambridge Conference on Fibre Optic Sensing in Civil Infrastructure, 30 June – 1 July 2014, Robinson College, University of Cambridge

2） Masaru Kamada: Cardinal splines in piecewise constant tension, 5th International Conference on Computational Harmonic Analysis, Vanderbilt University, Nashville, May 22, 2014.

【学会発表等(国内,国際)】

1) 宮坂隆平, 武田茂樹, 鹿子嶋憲一, 梅比良正弘, ″UHF帯RFIDによる災害時電子掲示板への情報伝達に関する検討,″ 電気学会東京支部茨城支所研究発表会, A13,pp.24-25, Nov. 2014.

2) Effect of internal cracking on mass transfer resistance of cover concrete, Okazaki, S., kurumatani, M., Ujike, I. and Takamoto, N.,Proceedings of Concrete Solutions, 5th International Conference on Concrete Repair, pp.683-690, 2014.

3) Toshiya Watanabe, Naohiro Ohtsuka, Susumu Shibusawa, Masaru Kamada, Tatsuhiro Yonekura, Design of lower limb chair exercise support system with depth sensor, The 11th IEEE International Conference on Ubiquitous Intelligence and Computing (UIC 2014), pp.104-111, Dec. 2014, Indonesia.

4) Toshiya Watanabe, Naohiro Ohtsuka, Susumu Shibusawa, Masaru Kamada, Tatsuhiro Yonekura, Motion detection and evaluation of chair exercise support system with depth image sensor, International Workshop on Future Trends in Computing System Technologies and Applications (FUSION 2014), pp.800-807, Dec. 2014, Indonesia.

5) 鎌田和樹, 渋沢進, 深度画像センサを用いた拮抗体操支援システム, 電子情報通信学会福祉情報工学研究会, Vol.114, No.357, WIT2014-66, pp.75-80, Dec. 2014, 東京.

6) 中屋隆, 澁澤進, Kinectセンサを用いた嚥下体操支援システム, 情報処理学会第162回ヒューマンコンピュータインタラクション研究会, March 2015, 東京.

7) Yuki Takahashi, Michitoshi Niibori and Masaru Kamada: NeighborNote: An Evernote application with capability of suggesting related notes based on user operation history, Proceedings of the 17th International Conference on Network-Based Information Systems(NBiS 2014), Salerno, Italy, 331-335 (Sep. 2014).

8) Yuto Yoshida, Michitoshi Niibori and Masaru Kamada: A business Log system to display related logs based on past cyclic events of business, Fifth International Workshop on Heterogeneous Networking Environments and Technologies (HETNET 2014), Proceedings of the 17th International Conference on Network-Based Information Systems(NBiS 2014), Salerno, Italy, 545-548 (Sep. 2014).

9) Erjing Zhou, Michitoshi Niibori, Shusuke Okamoto, Masaru Kamada and Tatsuhiro Yonekura: Interactive animation authoring platform based on state-transition diagrams that runs on Android devices, Third International Workshop on Web Service and Social Media (WSSSM 2014), Proceedings of the 17th International Conference on Network-Based Information Systems (NBiS 2014), Salerno, Italy, 596-599 (Sep. 2014).

10) Satoshi Kozawa, Michitoshi Niibori, Yasuhiro Ohtaki and Masaru Kamada:File manager that shows off notes out of the files, Third International Workshop on Web Service and Social Media (WSSSM 2014), Proceedings of the 17th International Conference on Network-Based Information Systems (NBiS 2014), Salerno, Italy, 611-614 (Sep. 2014).

11) Toshiya Watanabe, Naohiro Ohtsuka, Susumu Shibusawa, Masaru Kamada and Tatsuhiro Yonekura: Design of lower limb chair exercise support system with depth sensor, The 11th IEEE International Conference on Ubiquitous Intelligence and Computing (UIC 2014), Bali, Indonesia, pp.104-111, December 2014.

12) Toshiya Watanabe, Naohiro Ohtsuka, Susumu Shibusawa, Masaru Kamada and Tatsuhiro Yonekura: Motion detection and evaluation of chair exercise support system with depth image sensor, The International Workshop on Future Trends in Computing System Technologies and Applications (FUSION 2014), Bali, Indonesia, pp.800-807, December 2014.

13) Sachin Rai and Hiromasa Habuchi: Enhancement of Punctured Turbo Code with UTPA in Optical Wireless Channel, Proceeding of International Symposium on Information Theory and Its Applications (ISITA2014), Melbourne, Australia, Session:M-3-C (Coding Theory ¥& Practice I), pp. (2014-10-27)

14) Takuya Eto, Hiromasa Habuchi, and Koichiro Hashiura : Spread Spectrum/Binary Countdown Scheme with GMPSC for Multi-Hop Wireless Network, Proceeding of Eighth International Conference on Mobile Computing and Ubiquitous Networking (ICMU2015), Hakodate, Session:S2: Cognitive Radios and Ad Hoc Networks, (2015-1-20)

15) Sachin Rai, Yusuke Kozawa, Hiromasa Habuchi and Yuto Matsuda : Proposal of Turbo-Coded Differential OOK for Optical IM/DD System, Proceeding of 2015 RISP International Workshop on Nonlinear Circuits, Communications and Signal Processing, Kuala Lumpur, Malaysia, Session:Optical Communications, 28AM2-4-2, (2015-02-28)

16) 小澤佑介，羽渕裕真，楳田洋太郎 :マルチパルス PPM 方式を用いた光無線階層化変調法の性能解析，電子情報通信学会ワイドバンド研究会，名古屋工大，WBS2014-6, pp.31-36, 2014-05-16

17) 羽渕裕真，山形正哉 :変形擬 3 進 M 系列による M-ary 陪直交変調の同期追跡法， 電子情報通信学会ワイドバンド研究会，名古屋工大，WBS2014-7, pp.31-41, 2014-05-16

18) 江藤拓也，羽渕裕真，橋浦康一郎 :拡張プライム符号を用いる 2 進カウントダウン法の提案，電子情報通信学会ワイドバンド研究会，大阪市立大学文化交流センター，WBS2014-13(MICT2014-27), pp.23-27, 2014-07-29

19) 松田優人，羽渕裕真，小澤佑介 :同期信号を埋め込んだ差動符号化光 OOK の提案， 電子情報通信学会ワイドバンド研究会，大阪市立大学文化交流センター，WBS2014-14 (MICT2014-28), pp.29-32, 2014-07-29

20) ライサチン，羽渕裕真 : 光ワイヤレス通信における非均一電力割当型ターボ符号の誤り率特性，電子情報通信学会ワイドバンド研究会，大阪市立大学文化交流センター，WBS2014-20(MICT2014-34), pp.63-66, 2014-07-29

21) 村田直也，小澤佑介，楳田洋太郎，羽渕裕真 :一般化拡張プライム符号系列を用いた双方向可視光通信 LED-to-LED 方式に関する一検討，電子情報通信学会ワイドバンド研究会，大阪市立大学文化交流センター，WBS2014-21(MICT2014-35), pp.67-72, 2014-07-29

22) 江藤拓也，羽渕裕真，橋浦康一郎 :スペクトル拡散型 2 進カウントダウン法のスループットの一検討，電子情報通信学会ワイドバンド研究会，秋田県立大学カレッジプラザ，WBS2014-35, pp.19-22, 2014-10-03

23) 高橋貴大, 羽渕裕真, 小澤佑介: 光 MPPM-CNK のフレーム同期法の一検討, 電子情報通信学会ワイドバンド研究会, 秋田県立大学カレッジプラザ, WBS2014-37, pp.29-32, 2014-10-03

24) 高橋良介, 小澤佑介, 楳田洋太郎, 羽渕裕真 : 照明用LEDによる階層型MPPM-SIK方式の屋内位置に応じた誤り率特性の評価, 電子情報通信学会ワイドバンド研究会, 熊本大学, WBS2014-41, pp.13-18, 2014-12-18

25) 小磯翔, 羽渕裕真 : 誤り訂正符号を組み込んだ秘密分散法の検討, 電子情報通信学会東京支部学生研究発表会, 明治大, 24, 2015-02-28

26) 高柳翔太, 羽渕裕真, 高丸祐典 : 変形擬 3 進 M 系列を用いる光コードシフトキーイングの提案, 電子情報通信学会東京支部学生研究発表会, 明治大, 30, 2015-02-28

27) 細川勇気, 羽渕裕真 : 変形擬 3 進 M 系列対を用いる OFCDM の提案, 電子情報通信学会東京支部学生研究発表会, 明治大, 36, 2015-02-28

28) 松田優人, 羽渕裕真, 小澤佑介:差動符号化を用いる光無線 OOK の同期保持時間, 電子情報通信学会総合大会, A-5-5, 立命館大学, 2015-03-10(発表予定)

【採択された外部資金及び科学研究費補助金】

1) 科研費　挑戦的萌芽研究　（研究課題番号：26630215）
課題名　地盤中の水の挙動の調査を格段に進展できるワイヤレスマルチセンサの開発への挑戦
代表　風間基樹（東北大学）　分担　安原一哉，鎌田賢（茨城大学）
研究期間　2014 年 4 月 1 日～2017 年 3 月 31 日
研究費総額 4,915,000 円

2) 科研費　基盤研究（C）　（研究課題番号：26420409）
課題名　可変張力つき 2 変数スプラインの導出とその画像補間への応用
代表　鎌田賢（茨城大学）
研究期間　2014 年 4 月 1 日～2017 年 3 月 31 日
研究費総額　1,700,000 円

3)　モバイル端末による測位方法の検証に関する共同研究
期間　2013/11-2014/04
金額　250,000 円

4)　科研費　基盤研究(C)
課題名 センサネットワークと知識ベースを用いた高齢者見守りシステムの研究
代表 澁澤 進，H26 年度澁澤分 550 千円
研究期間　2012 年 4 月 1 日～2014 年 3 月 31 日
研究費総額　4,800,000 円

5)　科研費　基盤研究(C)
課題名 ITS のための光／電波融合型通信の高度化
代表 羽渕裕真，H26 年度 1100 千円
研究期間　2012 年 4 月 1 日～2015 年 3 月 31 日 研究費総額　4,200,000 円

6)　寄付金
帝人株式会社
課題名 高機能繊維材料の社会インフラにおける活用拡大、実用化に関する研究
代表 呉智深，H26 年度 500 千円

7)　寄付金
株式会社ＫＳＫ
課題名 「中小企業・小規模事業者ものづくり・商業・サービス革新事業（専門家指導）
代表 呉智深，H26 年度 1000 千円

8)　寄付金
特定非営利活動法人 光防災センシング振興協会
課題名 河川堤防の変状検知等モニタリングシステムの技術研究開発（国交省プロジェクト）
代表 呉智深，Ｈ２６年から５年間

【地域社会活動】

1) 齋藤　修：ひたちなか市外野小学校等における理科教育の支援の一環として、理科・環

境・情報等の総合的教育を行った（2014 年 11 月～2015 年 2 月）。

2) 鎌田　賢：第 38 回全国高等学校総合文化祭「いばらき総文祭 2014」コンピュータ部門のプログラミングコンテストにおいて、予選・本選（平成 26 年 7 月 28 日（月）29 日（火））の審査委員を務めた。本選ではデモ展示も行った。

茨城大学工学部附属防災セキュリティ技術教育研究センター　（2014 年度）

呉　　智深　　（工学部都市システム工学科・教授・センター長）
齋藤　　修　　（防災セキュリティ教育研究センター・特命教授・副センター長）
鎌田　　賢　　（工学部情報工学科・教授・副センター長）
桑原　祐史　　（広域水圏環境科学教育研究センター・准教授・センター幹事）
沼尾　達弥　　（工学部都市システム工学科・教授）
今井　　洋　　（工学部電気電子工学科・教授）
原田　隆郎　　（工学部都市システム工学科・准教授）
横田　浩久　　（工学部電気電子工学科・准教授）
湊　　　淳　　（理工学研究科・教授）
武田　茂樹　　（工学部メディア通信工学科・教授）
澁澤　　進　　（工学部情報工学科・教授）
羽渕　裕真　　（工学部情報工学科・教授）
外岡　秀行　　（工学部情報工学科・准教授）
車谷　麻緒　　（工学部都市システム工学科・准教授）

茨城大学重点研究

「知的で持続可能な社会基盤および防災セキュリティ技術研究創出

事業」

茨城大学工学部附属防災セキュリティ技術教育研究センター

２０１４年度報告書

発行日　　　平成 27 年 4 月

発行者　　　茨城大学　工学部　都市システム工学科
教授　呉　智深
〒316-8511 日立市中成沢町 4-12-1
Tel: 0294-38-5179　Fax: 0294-38-5268

茨城大学重点研究
http://www.ibaraki.ac.jp/generalinfo/activity/researching/juuten/

茨城大学工学部附属教育研究センター
http://www.eng.ibaraki.ac.jp/research/centers/index.html

防災セキュリティ技術教育研究センター
http://www.eng.ibaraki.ac.jp/research/centers/disaster/index.html